RESEARCH ARTICLE

Key Points:
- New observations of aseismic slip along a segment of a major plate boundary (El Pilar fault, Venezuela)
- Evidence of spatial and temporal variations in creep over the 2007–2011 period
- Creep occurs on the segment ruptured in 1997, it corresponds to an afterslip which evolved into interseismic creep showing transients

Supporting Information:
- Supporting Information S1

Correspondence to:
L. Pousse Beltran,
poussela@gmail.com

Spatial and temporal variations in creep rate along the El Pilar fault at the Caribbean-South American plate boundary (Venezuela), from InSAR

Léa Pousse Beltran[1], Erwan Pathier[2], François Jouanne[1], Riccardo Vassallo[1], Carlos Reinoza[3], Franck Audemard[3], Marie Pierre Doin[4], and Matthieu Volat[4]

[1]ISTerre, Université de Savoie Mont Blanc, Le Bourget du Lac, France, [2]ISTerre, Université Grenoble Alpes, Grenoble, France, [3]Venezuelan Foundation for Seismological Research, Caracas, Venezuela, [4]ISTerre, CNRS, Grenoble, France

Abstract In eastern Venezuela, the Caribbean-South American plate boundary follows the El Pilar fault system. Previous studies based on three GPS campaigns (2003–2005–2013) demonstrated that the El Pilar fault accommodates the whole relative displacement between the two tectonic plates (20 mm/yr) and proposed that 50–60% of the slip is aseismic. In order to quantify the possible variations of the aseismic creep in time and space, we conducted an interferometric synthetic aperture radar (InSAR) time series analysis, using the (NSBAS) New Small BAseline Subset method, on 18 images from the Advanced Land Observing Satellite (ALOS-1) satellite spanning the 2007–2011 period. During this 3.5 year period, InSAR observations show that aseismic slip decreases eastward along the fault: the creep rate of the western segment reaches 25.3 ± 9.4 mm/yr on average, compared to 13.4 ± 6.9 mm/yr on average for the eastern segment. This is interpreted, through slip distribution models, as being related to coupled and uncoupled areas between the surface and ~ 20 km in depth. InSAR observations also show significant temporal creep rate variations (accelerations) during the considered time span along the western segment. The transient behavior of the creep is not consistent with typical postseismic afterslip following the 1997 M_s 6.8 earthquake. The creep is thus interpreted as persistent aseismic slip during an interseismic period, which has a pulse- or transient-like behavior.

1. Introduction

Shallow fault creep can be detected by measurement of localized aseismic displacement gradients crossing faults [e.g., *Thatcher*, 1979]. This shallow creep is common during a postseismic period, as localized afterslip phenomena, but it can also exist during the interseismic period, as observed on the San Andreas fault system, Haiyuan fault in China, North Anatolian fault, and the Longitudinal Valley fault of Taiwan among others [e.g., *Schmidt et al.*, 2005; *Cavalié et al.*, 2008; *Champenois et al.*, 2012; *Kaneko et al.*, 2013; *Lindsey et al.*, 2014]. *Avouac* [2015] reviewed key factors controlling aseismic slip. This slip can depend on lithology [e.g., *Wei et al.*, 2013; *Thomas et al.*, 2014a] or can be related to the fault geometry [e.g., *Jolivet et al.*, 2013; *Lindsey et al.*, 2014]. The influence of thermal control and fluid pressure on slip-mode processes has also been proposed (e.g., respectively, *Blanpied et al.* [1991] and *Gratier et al.* [2011]. In addition, previous seismic ruptures have an influence on the subsequent slip-mode processes [e.g., *Zweck et al.*, 2002; *Çakir et al.*, 2003]. However, the relative contributions of these different factors in controlling aseismic slip remain poorly understood, especially since spatiotemporal variations of aseismic slip have been detected [e.g., *Wei et al.*, 2009; *Barbot et al.*, 2013; *Jolivet et al.*, 2013; *Cetin et al.*, 2014; *Thomas et al.*, 2014b; *Khoshmanesh et al.*, 2015; *Turner et al.*, 2015]. More case studies of faults showing spatial and temporal variations in creep, from a range of different geodynamic and geological contexts, are thus needed to unravel the causes and implications of aseismic slip. Since both steady and unsteady aseismic slips affect stress accumulation on a fault, it is important these processes are taken into account the assessment of slip deficit and seismic hazard [*Ryder and Bürgmann*, 2008; *Shirzaei and Bürgmann*, 2013; *Shirzaei et al.*, 2013]. In this study, we present new observations of temporal and spatial variations along the El Pilar fault system, which is part of the Caribbean-South American plate boundary.

The E-W dextral strike-slip El Pilar fault, which accommodates almost all of the 20 mm/yr relative displacement between the Caribbean and South American plates (Figure 1) [*Weber et al.*, 2001; *Jouanne et al.*, 2011], is an interesting case study for analyzing the relationship between aseismic and seismic slip modes.
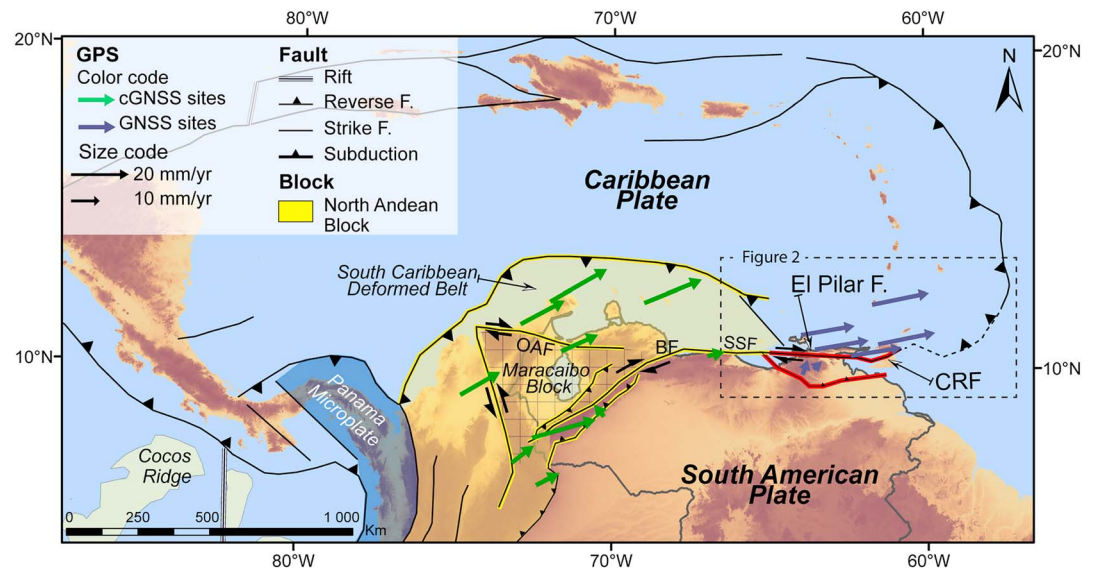
Figure 1. Geodynamic map of the Caribbean/South American plates. Arrows are GNSS (Global Navigation Satellite Systems) velocities in the Caribbean region with respect to a fixed South American plate, calculated by *Reinoza* [2014]. Green arrows represent velocities measured on permanent GNSS sites (cGNSS) from the FUNVISIS, REMOS-IGVSB, and GEORED networks. Blue arrows represent velocities derived from episodic GNSS data measured in 2003–2005 and 2013 [*Reinoza*, 2014]. Yellow and red lines are fault systems that represent, respectively, the western and eastern plate boundary systems in Venezuela. The GNSS velocity field shows that the El Pilar fault accommodates all the relative displacement between the Caribbean and South American plates. Plate boundary mapping is based on *Beltran* [1993], *Audemard et al.* [2000], *Pindell et al.* [2006], and *Audemard* [2009]. DEMs are from the USGS [*Rabus et al.*, 2003]. CRF, Central Range fault; SSF, San Sebastian fault; OAF, Ocá-Ancón fault; and BF, Boconó fault.

Seismicity, paleoseismology, and geodesy indicate that this fault exhibits seismic as well as aseismic behavior [*Audemard*, 2006, 2007; *Reinoza et al.*, 2015]. For example, the El Pilar fault produced seismic events in 1684, 1797, 1853, 1929, and 9 July 1997 [*Audemard*, 1999, 2006, 2007, 2011; *Altez and Audemard*, 2008; *Aguilar et al.*, 2016]. In addition, aseismic slip has been detected through field observations, episodic measurements performed in 2003, 2005, and 2013 on a sparse network of 32 GNSS (Global Navigation Satellite Systems) stations, and measurements of one continuous GNSS station [*Audemard*, 2006; *Jouanne et al.*, 2011; *Reinoza et al.*, 2015]. Despite the low resolution in space and time, *Reinoza et al.* [2015] showed that, in the seismogenic layer (0–12 km depth), between 40 and 50% of the fault area is locked, and that the aseismic slip is certainly not spatially uniform.

However, measurements with better spatial and temporal resolution are needed to answer a number of remaining questions. Near field data can improve the spatial resolution of aseismic slip mapping and help identify potential segmentation of creep, as proposed by *Jouanne et al.* [2011] and *Reinoza et al.* [2015]. Denser and longer geodetic time series would also improve our knowledge about the creeping process, for instance, by distinguishing the nature of the creep: e.g., afterslip induced by the latest seismic event in 1997 (M_s 6.8) which has transitioned into a persistent interseismic slip or an afterslip which is still occurring. We would like to understand the local observation of slip acceleration in 2002 [*Jouanne et al.*, 2011] and the inconsistency between the return periods evaluated in trenches at 400 years [*Audemard*, 2011] and the return period estimated at up to 200 years, assuming a geological slip rate of 20 mm/yr and a characteristic slip of 1 to 4 m slip (coseismic slip and afterslip) [*Pérez et al.*, 2001; *Jouanne et al.*, 2011]. Finally, higher spatial resolution can also help to detect asperities that may trigger events like the M_s 6.8 in 1997 [e.g., *Chaussard et al.*, 2015a, 2015b; *Jolivet et al.*, 2015a].

This paper presents an analysis of 18 SAR (synthetic aperture radar) images from the L band Advanced Land Observing Satellite (ALOS-1) satellite spanning the 2007–2011 period using the spaceborne SAR interferometry technique (interferometric synthetic aperture radar, InSAR). These images, processed with the NSBAS method [*Doin et al.*, 2011], provide a coverage at high spatial and temporal resolution for the onshore section of the El Pilar fault and allow us to identify spatio temporal slip variations along the fault. In the last part of the
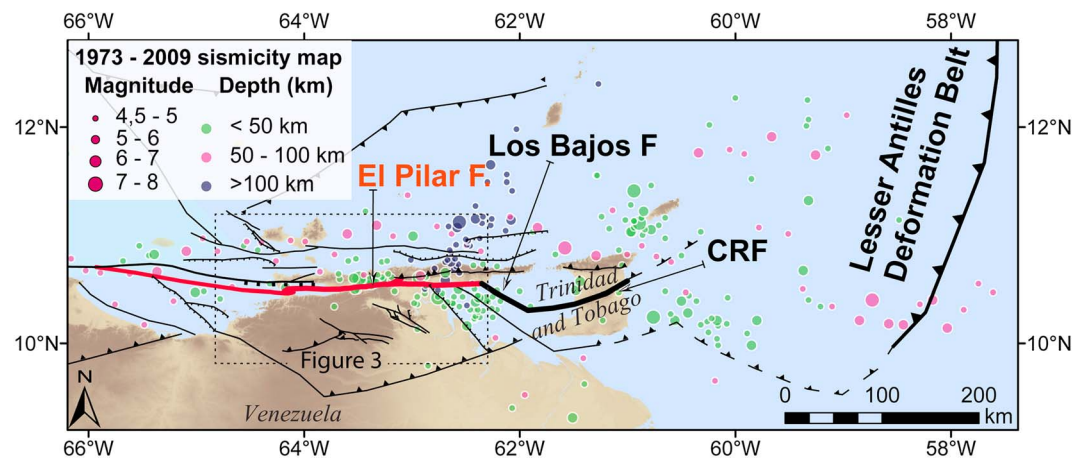
Figure 2. Seismotectonic map. In eastern Venezuela the major E-W relative displacement between the Caribbean and South American plates is accommodated along the El Pilar fault (in red). This fault is constituted by several segments onshore and offshore. Thrusts and reverse faults south of the El Pilar fault accommodate the minor N-S component of the relative displacement between the Caribbean and South American plates in Venezuela. Deep seismicity (in blue and purple) related to the Lesser Antilles subduction ends abruptly along dextral faults. Fault mapping is based on *FUNVISIS* [1994], *Audemard et al.* [2000], and on *Audemard* [2009]. The 1973–2009 seismicity data are provided by GeoMap App http://www.geomapapp.org/ [*Ryan et al.*, 2009]. CRF, Central Range fault.

paper we discuss the segmentation of the El Pilar fault and the relationship between aseismic slip and seismicity, and the implications for seismic hazard assessment.

2. The El Pilar Fault System: Seismotectonic and Geological Context

The Caribbean-South American plate boundary is a transpressional zone characterized by a complex system: distributed faults in the west (yellow thick lines in Figure 1) and a localized fault system in the east (red lines in Figure 1). GPS studies indicate ~ 2 cm/yr eastward motion of the Caribbean plate with respect to a fixed South American plate [*Pérez et al.*, 2001; *Weber et al.*, 2001; *DeMets et al.*, 2010]. In the eastern part of the plate boundary, neotectonic studies have shown the existence of strain partitioning: the major E-W component is accommodated by a tectonic boundary composed of several right-lateral faults (El Pilar, Los Bajos, and Central Range faults) [*Beltran et al.*, 1996; *Audemard and Audemard*, 2002], whereas the minor oblique or N-S component is accommodated by active thrusting to the south (Figures 1 and 2) with vertical deformation rates of 0.6 to 0.1 mm/yr [*Fajardo*, 2015]. Moreover, the seismicity related to the Lesser Antilles subduction ends abruptly along dextral faults, which suggests a tectonic relationship between both systems due to the tearing of the Lesser Antilles subducted oceanic lithosphere (Figure 2) [*Pérez and Aggarwal*, 1981; *Clark et al.*, 2008; *Audemard*, 2009].

The El Pilar fault, which belongs to the E-W dextral system, crosscuts a Mesozoic thrust system separating two contrasting Mesozoic terrains: a northern province consisting of low-grade metasediments associated with oceanic crustal remnants (schist, quartzite, and serpentine lenses) and a southern province made of non metamorphosed sediments (Figure 3) [*Metz*, 1965; *Vignali*, 1977; *Vierbuchen*, 1984; *Jacome et al.*, 1999]. Variations of elastic properties would also be expected across this tectonic boundary, as suggested by *Reinoza et al.* [2015]. The El Pilar fault is composed of several structural segments, defined by neotectonic analyses [*Beltran et al.*, 1996; *Audemard et al.*, 2000; *Van Daele et al.*, 2011]. Based on the joint interpretation of seismic, magnetic, and gravimetric data *Hernandez et al.* [1987] suggested a seismogenic depth of 15 to 20 km. Segmentation, 1997 rupture plane area, and dip changes (65° northward, to vertical, to 75° southward) of the upper part of the fault were investigated through the analysis of aftershocks following the 1997 M_S 6.8 event which were mainly located between the surface and 14 km depth [*Baumbach et al.*, 2004].

These geological and geometrical constraints were used by *Jouanne et al.* [2011] and *Reinoza et al.*, [2015] to explain, through modeling, the observed asymmetric velocity gradients on both sides of the fault and the high displacement gradient crossing the fault. They investigate different modeling approaches, and their results suggest the existence of spatial variations of interseismic coupling at seismogenic depths. However,
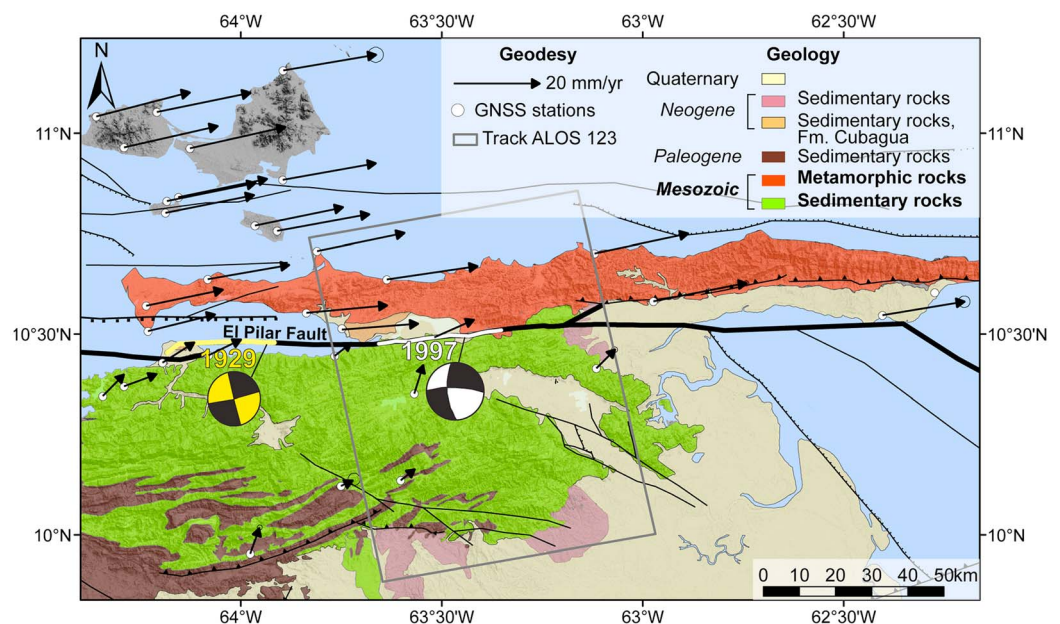
Figure 3. Schematic geological map and geodetic surveys of the El Pilar fault region. The block to the north of the fault is composed of Mesozoic metamorphosed sediments and oceanic remnants (schist, quartzite, and serpentines lenses), while to the south it is composed of Mesozoic non metamorphosed sediments [*Vignali*, 1977; *de Juana et al.*, 1980; *Vierbuchen*, 1984; *Hackley et al.*, 2005]. White dots are GNSS station. Black arrows are interseismic velocities estimated with GNSS data (considering a fixed South American plate) [*Reinoza et al.*, 2015]. The rectangle is the shape of the InSAR ALOS-1 ascending track A123. Surface ruptures of the 1929 and 1997 events are, respectively, plotted as yellow and white lines, with their respective focal mechanisms [from *Baumbach et al.*, 2004]. Faults mapping come from *Audemard et al.* [2000].

their results were limited by the sparsity of the geodetic network and the availability of only three GNSS campaign (2003, 2005, and 2013) and just one continuous GNSS station.

3. Interferometric Synthetic Aperture Radar (InSAR) Processing

To mitigate InSAR temporal decorrelation due to the dense Venezuelan equatorial vegetation cover, we used L band (23.6 cm wavelength) images from Advanced Land Observing Satellite (ALOS-1, JAXA), which gives better results than the C band or X band images in this type of environment [*Wei and Sandwell*, 2010] (several tests in this area performed with Sentinel-1A data yielded interferograms with less coherence than with ALOS data). ALOS SAR images were processed in Fine Beam Single polarization mode or in Fine Beam Dual polarization mode but using only the HH polarization, resampled at a spatial resolution of ~10 m. These images were acquired along the ALOS ascending track A123, frame 190. Eighteen SAR images spanning the 2007–2011 period (16 June 2007 to 2 September 2011) were used to form 73 differential interferograms with the NSBAS processing chain [*Doin et al.*, 2011] based on the ROI-PAC software [*Rosen et al.*, 2004]. The Shuttle Radar Topography Mission digital elevation model (DEM) at 3 arc sec resolution [*Rabus et al.*, 2003], resampled at 45 m resolution, has been used to accurately coregister the focused SAR images and to correct interferograms from the topographic contribution to the interferometric phase. The interferogram network and examples of unfiltered and uncorrected interferograms are provided in the supporting information (Figures S1 and S2). European Centre for Median-Range Weather Forecast ERAI (ERAInterim) atmospheric reanalysis was used to correct atmospheric delay [*Doin et al.*, 2009; *Jolivet et al.*, 2011]. DEM errors were corrected on interferograms following the method of *Ducret et al.* [2014]. Before unwrapping, two kinds of filter were used with a spatial window of about 180 m: the adaptive filter of *Goldstein et al.* [1988] and the adaptive weighted filter of *Doin et al.* [2011].

In some unfiltered and unwrapped interferograms a clear phase jump is visible across the fault (see Figure S2); however, the time series analysis greatly improves the measurements. Another distinctive feature in the interferograms is the swamps where the interferometric phase maintains high coherence
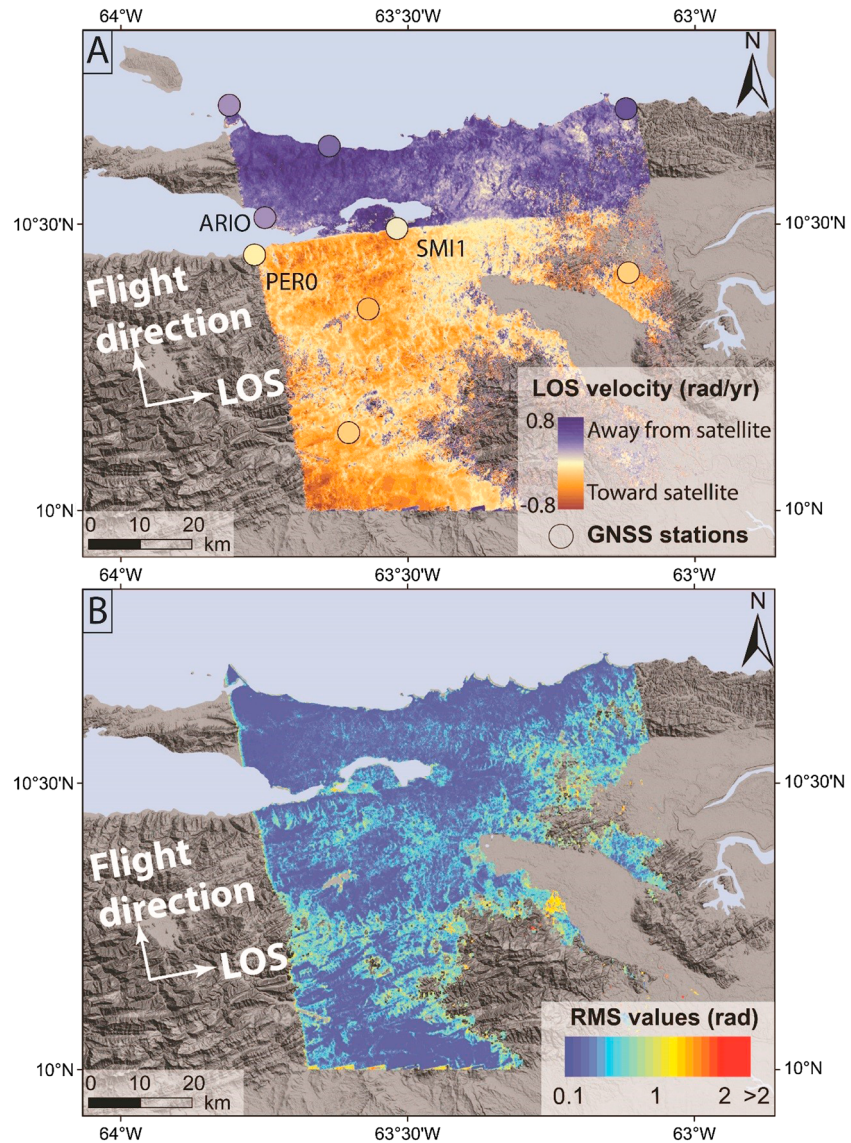
Figure 4. InSAR processing results for ascending track A123. (a) The 30 m resolution InSAR line-of-sight velocities estimated over 3.5 years (2007–2011). Dots are GNSS stations, the dot colors also represent GNSS horizontal projected in LOS (same color scale as InSAR). (b) RMS values map for each pixel, estimated over 3.5 years (2007–2011): close to swamps and in the east RMS values can exceed 0.5 rad. (ALOS-1 data distributed by Japan Space Systems © Ministry of Economy, Trade, and Industry and Japan Aerospace Exploration Agency).

and for which local fringes are detected. This is likely due to water level change (see Figure S3 in the supporting information). This pattern has been already observed in wetland areas and used to measure water level changes or subsidence [*Alsdorf et al.*, 2000; *Kim et al.*, 2009; *Chaussard et al.*, 2013]. To avoid unwrapping issues due to these fringes, we chose to mask them. Unwrapping was performed in 2-D with the NSBAS chain using a method similar than in *Doin et al.* [2015]. The unwrapped interferograms were then systematically visually checked. When large unwrapping errors were detected, we used a manual bridge between coherent areas to correct them as explained in *Doin et al.* [2011] and *Grandin et al.* [2012] (Figure S4 in the supporting information).

To obtain a map of ground velocity along the line-of-sight (LOS) direction (Figure 4a) and a cumulative displacement map along the LOS for each date of acquisition, we applied a time series analysis using a model based on *López-Quiroz et al.*, [2009], *Doin et al.* [2011], and *Jolivet et al.* [2012]. The final pixel size of our maps is approximately 30 m. The root-mean-square (RMS) on each pixel is given by the time series analysis model
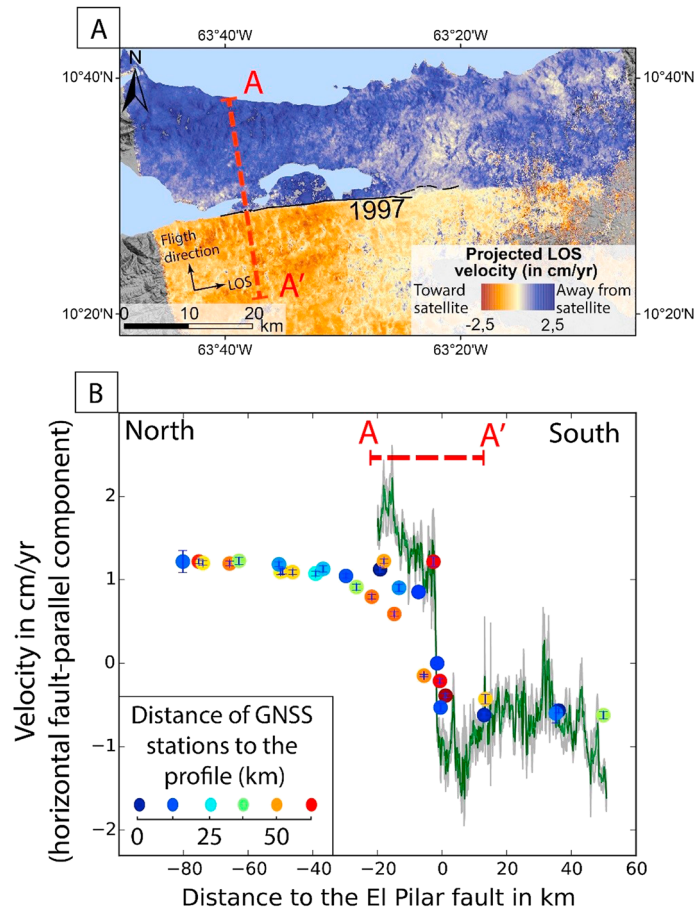
Figure 5. (a) The black line is the 1997 surface rupture [*Audemard*, 2006]. The red line (A–A') gives the location of the profile shown in Figure 5b. (b) GPS and INSAR velocity field profile across the El Pilar fault (A–A'). Dots correspond to GNSS velocities for the stations shown in Figure 3 [*Reinoza et al.*, 2015] projected along the A–A' profile (we keep GNSS stations situated up to 100 km of the A–A' profile). Dot color scale represents the distance between the GNSS stations and the profile. The green curve shows INSAR velocity (weighted average over 16 pixels (480 m) width across the profile) with 1 sigma deviation (gray zone). INSAR velocities have been converted to give an equivalent horizontal fault-parallel component velocities, and GNSS velocities are also given for the same component.

(Figure 4b) and is calculated "between the observed interferogram phase and the one reconstructed from inverted successive phase delays" [*López-Quiroz et al.*, 2009]. This RMS value is an estimation of the accuracy of the inversion scheme and gives a quality value for the LOS displacement or velocity for each pixel, which can be used to weight these data. For instance, in the following figures of this paper showing velocity profiles, plotted velocities are a weighted average of 16 pixels (that is 480 m) across the profile, with ±1 sigma deviation shown in gray (see Figure 5 for example).

Due to the limited number of images available (18), a velocity map output from NSBAS may be affected by residual atmospheric, ionospheric, or orbital errors, producing a long wavelength signal. Indeed, our raw velocity map shows a residual ramp mainly in the range direction (Figure S5), which is almost parallel to the El Pilar fault. Such a signal is not seen in velocity fields derived from GNSS (Figure 4a). We remove this signal using a linear function in the radar range and azimuth direction. This deramping function ($ax + by + c$) is estimated in order to minimize the difference between the nine GNSS velocities measured within the boundaries of the InSAR track and InSAR velocities. The GNSS velocities are relative the SMI1 station. GNSS velocities are projected into the local satellite LOS (line of sight), and InSAR velocities are averaged in a circus of 2 km radius around every GNSS stations (Figure 4a). The choice of a simple deramping function was guided by the low number of GNSS stations covered by the track. It is important to note that this ramp correction does not affect the localized (<10 km) phase jump across the fault.

The lack of data acquired along descending tracks does not allow vertical velocity to be estimated. Assuming that the El Pilar fault is a pure strike-slip fault with no vertical component and that ground displacement is essentially in the fault-parallel direction, we project LOS InSAR data onto the horizontal surface for all the following figures of this paper in order to facilitate interpretations. Neglecting the vertical component is mainly justified by GNSS observations [*Jouanne et al.*, 2011; *Reinoza et al.*, 2015] and by field observations gathered along the surface rupture of the 1997 earthquake [*Audemard*, 2006]. We convert the LOS velocities in fault-parallel horizontal component velocities taking into account the variation of incidence and azimuth angles along the SAR data swath.

4. InSAR Inversion Results

4.1. Spatial Variation of Creep Rate

On the InSAR velocity map from 2007 and 2011, there is a sharp and linear velocity jump (E-W boundary between yellow and blue areas in Figures 4a and 5a corresponding, respectively, to relative displacements away from and toward the satellite). Visual comparison between the sharp boundary and the surface rupture of the 1997 earthquake mapped in detail by *Audemard* [2006] shows very good agreement (Figure 5a), within the limits of InSAR resolution and map uncertainties (<200 m). Furthermore, this sharp boundary continues away from the 1997 surface rupture and follows the El Pilar fault geological trace mapped by *Beltran et al.* [1996]. Those observations strongly suggest that the velocity boundary can be interpreted by the presence of creep along the El Pilar fault, at least in its shallowest part.

The InSAR velocity profile (A–A') across the fault in Figure 5 shows clearly the velocity jump located at the fault trace. To compare GNSS and InSAR signals, all horizontal GNSS velocities (in fault-parallel component) from *Reinoza et al.* [2015] (plotted in Figure 3) were projected onto the profile. On this profile plotted in Figure 5, the jump across the fault is slightly higher in 2007–2011 InSAR velocities than in 2003–2005–2013 GNSS velocities. The slight differences between both kinds of data can be explained by (1) different acquisition periods: 2007–2011 period for average InSAR velocities and 2003–2005–2013 acquisition campaigns for GNSS velocities (see discussion in 6.3), (2) the vertical components which are not taken into account (not estimated in the InSAR velocity map), and (3) GPS velocity projections onto the profile, e.g., some GNSS stations are located 50 km away from the A–A' profile where InSAR velocities are sampled in Figure 5.

Other InSAR velocity profiles across the fault show a large and abrupt step crossing the fault (Figure 6). As plotted on these profiles, the velocity step across the fault does not correlate with the topography. To quantify the step and the distance over which the step occurs, we fitted the InSAR velocity values to the following mathematical function, which is able to represent the main characteristics of our observed profiles (Figures 6 and S6 in the supporting information; the functions have been adapted from *Larson et al.* [2004] who use it for time series):

$$v(x) = v_0 + \frac{U}{2}\left(\tanh\left(\frac{x - X_0}{D}\right) - 1\right) + R * x \qquad (1)$$

In this equation, x is the perpendicular distance to the fault (the x axis of the profile), $v(x)$ is the velocity at x, v_0 is the far field velocity, U is the velocity value corresponding to the step, X_0 is the median position of the large step, D is the distribution that describes the distance over which the step is measured, and R accounts for a possible velocity ramp along the section. In profiles crossing the fault, the velocity step between the northern and the southern blocks can be fitted by equation (1) (e.g., in Figure S6). Parameters and standard deviation errors are estimated from non linear least squares adjustment using the Levenberg-Marquardt algorithm [*Levenberg*, 1944; *Marquardt*, 1963]. To compare the fit quality of each profile, we performed a χ^2 statistical test which provides an estimation of the robustness of the fit. The advantage of this method is to provide an estimation for the step distribution (D in equation (1)), to evaluate the uncertainties on each unknown parameter, and to remove, through the R term in equation (1), the possible contribution of long wavelength residual orbital errors or atmospheric signals which have not been corrected in the azimuth direction (see section 3).

Using the mean velocity map over the 2007–2011 period, InSAR velocities were sampled across the fault along 94 profiles with 480 m spacing. Each profile is 3.4 km long and 480 m wide; they do not overlap.
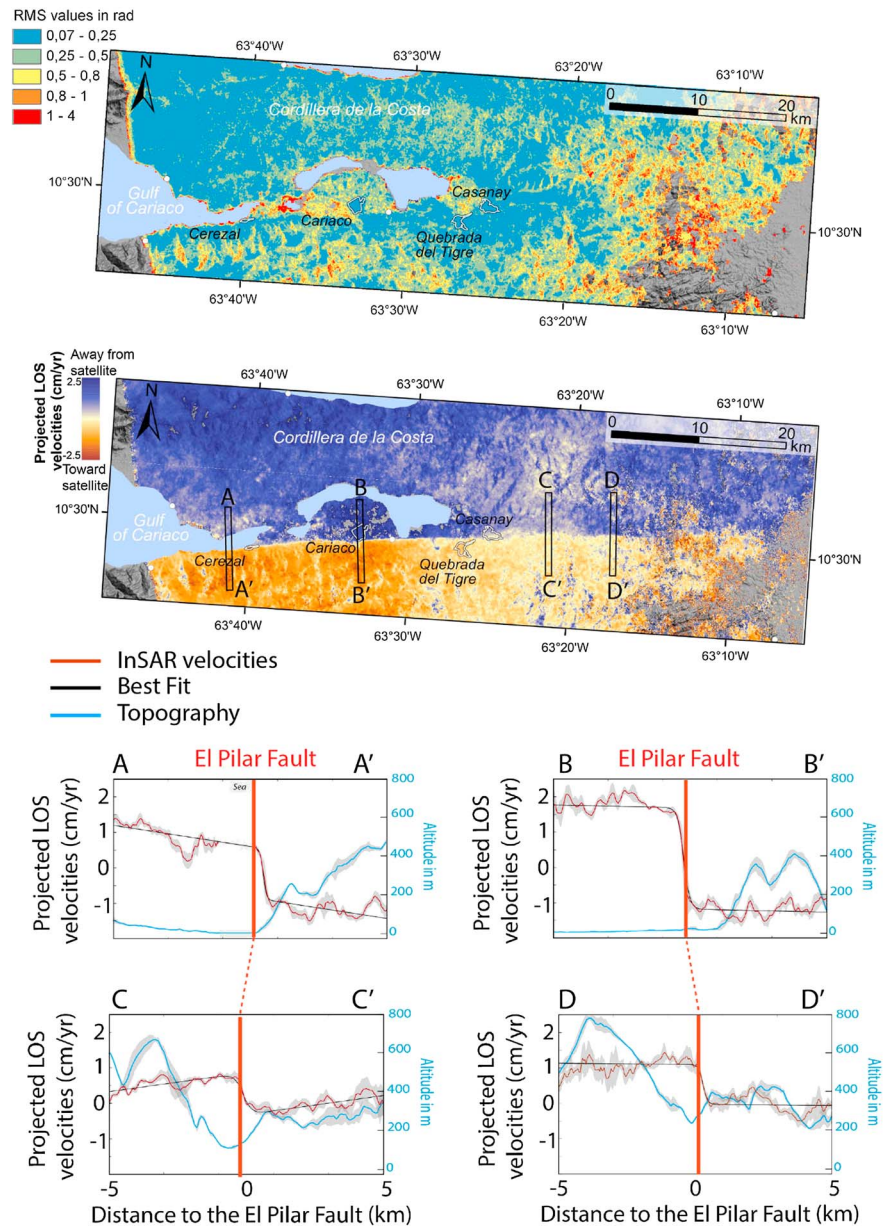
Figure 6. InSAR velocity map (2007–2011 period) and associated uncertainties. AA', BB', CC', and DD' are fault-perpendicular profiles, the red line indicates the position of the fault trace. Each plot displays the topography (blue line), the InSAR velocities projected onto the horizontal fault-parallel direction (weighted average over 16 pixels width (or 480 m)) (dark red line), 1 sigma deviation (gray zone), and the best fit of InSAR velocity values by the equation (1) (black line).

Profiles are then fitted by 1. Using this method, it appears that velocity steps vary along the El Pilar fault (Figure 7a). Between 63°42'W and 63°30'W along the fault the step regularly increases from ~13 mm/yr to ~40 mm/yr. In contrast, eastward of longitude 63°28'W, the step is lower, with a more constant value of about 13.4 ± 7.3 mm/yr. Unfortunately, the transition between these two portions of the fault is masked by the presence of swamps. Based on this geodetic contrast, hereafter in the paper, we propose to distinguish two "segments" (see Figure 7), separated at longitude 63°28'W. From a tectonic point of view this division point corresponds to a small fault step over [*Beltran et al.*, 1996; *Baumbach et al.*, 2004; *Audemard*, 2006]. *Baumbach et al.* [2004] do not recognize this step over as a major fault segment boundary (in their map of the fault trace our boundary corresponds to the middle of their segment 3). According to their map, one may argue that the limit could instead be defined at longitude 63°25'W,
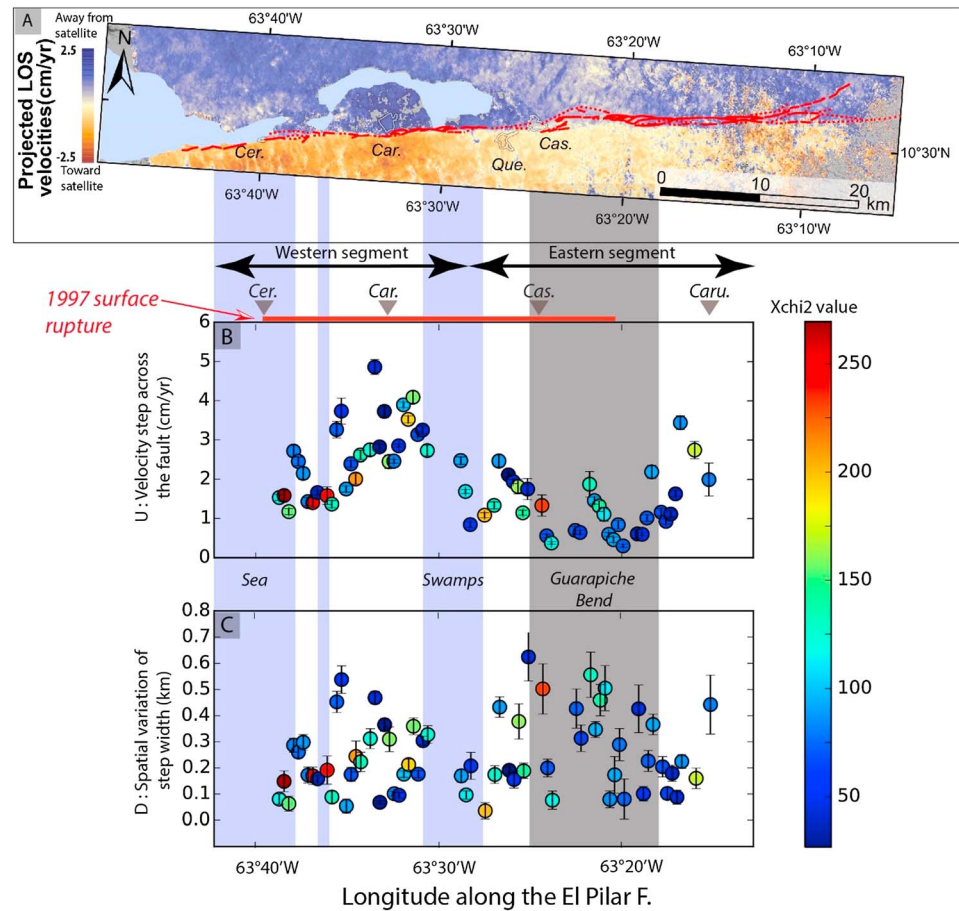
Figure 7. (a) InSAR mean velocity map (2007–2011 period), the El Pilar fault mapping of *Beltran et al.* [1996] is shown in red. Car., city of Cariaco; Que., Quebrada del Tigre; Cas., Casanay; and Caru., Carupano. (b) Spatial variation of velocity steps across the fault (U in equation (1)), as a function of longitude along the fault. (c) Spatial variation of step width (*D* in equation (1)), as a function of distance along the fault. For each estimation, the standard deviation (error bars) and the $\chi2$ value (dot colors) are plotted.

corresponding to the Guarapiche fault bend. Nevertheless, our following analysis and conclusions remain valid for both definitions.

Regarding the distribution of the deformation across the fault, Figure 7b shows that most of the steps across the fault are distributed over less than 500 m. The velocity steps are thus essentially extremely localized, and this indicates that at least the shallow part of the fault is creeping, as suggested by *Reinoza et al.* [2015]. It should be noted that the step width estimation is limited at its lower boundary not only by the spatial resolution of the InSAR velocity map, which is 30 m, but also by the prior interferogram filtering done on the basis of 6 pixel size windows, which is 180 m (see section 3). Taking that limit into account, it is likely that in some places the creep could reach the surface, which is supported by field observations [*Audemard*, 2006; *Jouanne et al.*, 2011].

4.2. Temporal Variation of Creep Rate

To estimate the temporal variations of the velocity steps across the fault, we follow the same method applied to the mean velocity map but applied to each time step of the smooth cumulative displacement time series. Using cumulative displacement profiles across the fault (same profile characteristics as in the section 4.1), displacement steps at the fault are estimated using equation (1) for each time increment (i.e., between two consecutive acquisition dates of SAR images) and are converted into incremental velocity steps (Figure 8). Some dates, for instance, 19 December 2008, contain profiles, which are too noisy to be fitted by equation (1), and explain the numerous gaps in velocity step estimations in Figure 8.
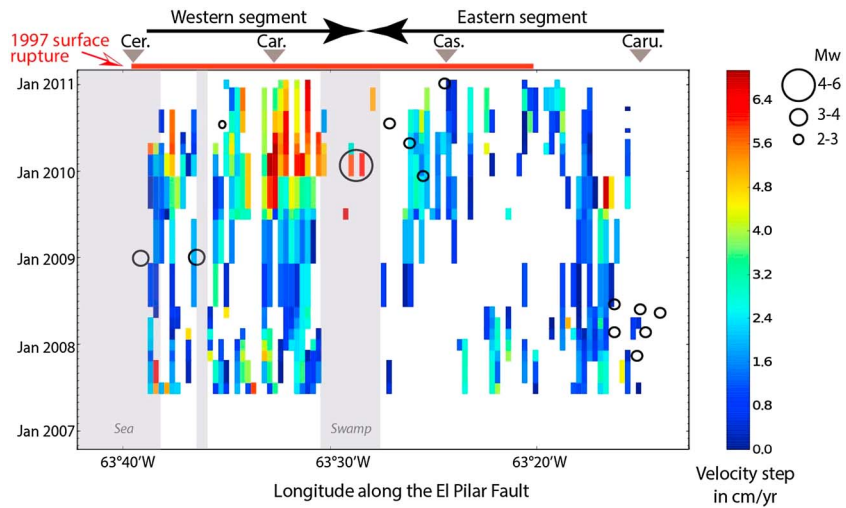
Figure 8. Velocity steps across the fault calculated between two consecutive dates; white area corresponds to areas where cumulative displacement could not be estimated. Black dots correspond to the seismicity provided by the *International Seismological Centre* [2013] ($M_w > 2$). There is no clear general correlation between seismicity and creep rate increases. One sigma deviation of the creep rate is shown in Figure S7 in the supporting information. Car., city of Cariaco; Que., Quebrada del Tigre; Cas., Casanay; and Caru., Carupano.

Comparing the velocity step variations along the fault and earthquakes ($M_w > 2$) recorded between 2007 and 2011 (Figure 8), we do not observe a clear spatial and temporal correlation between velocity step variations and the occurrence of these events, which means that the observed creep is mostly aseismic. The main seismic event is the January 2010 earthquake (M_w 5.5 at 2.4 km depth) with a dextral focal mechanism [*FUNVISIS*, 2010] which will be discussed below in section 6.2. Regarding the distribution of the deformation (parameter *D* in (1)), despite some noisy data, our results indicate that the deformation width remains stable through time, localized over less than 1 km (see Figure S8 in the supporting information).

Along the western segment, for each time interval, a spatial variation of the cumulative displacement steps across the fault is observed. In addition to these spatial variations, for each profile across the fault, we can see a temporal variation of the creep rate. It should be noted that short-term variations cannot be detected due to the low temporal sampling of ALOS-1 data (ranging from 1 to 6 months, see Figure S1 and Table S1 in the supporting information). According to our analyses, two phases can be distinguished (Figure 9a). Although the beginnings and endings of each phase are not well constrained due to the low temporal sampling, the two phases can be defined as Phase I between June 2007 and June 2009, with an average velocity of 15.2 ± 6.4 mm/yr, and Phase II from June 2009 to February 2011, during which time average velocity significantly increased and reached 30.2 ± 18.0 mm/yr. Such an acceleration has been already observed in the field based on measurements of local displacement markers during the 2002–2003 period following the 1997 earthquake [*Audemard*, 2006; *Jouanne et al.*, 2011]. Velocities during the Phase II locally are higher than the relative plate motions [*Pérez et al.*, 2001; *Weber et al.*, 2001; *DeMets et al.*, 2010]. This strongly suggests that it is a transient phenomenon.

No significant temporal variation in the velocity step is detected on the eastern segment (Figure 9b). We can notice that there is an exception for two profiles that cannot be included in the western segment which seem to be affected by similar temporal variations. However, these exceptions are isolated, and our conclusions remain valid. The step seems to be constant at 13.4 ± 6.9 mm/yr over the time period from 2007 to 2011 (which is consistent with the rate of 13.4 ± 7.3 mm/yr found in the mean velocity map over the 2007–2011 period).

5. Slip Distribution Model

Among the numerical models performed by *Reinoza et al.* [2015], their slip distribution inversion shows that the interseismic aseismic slip is not uniform in the seismogenic layer. However, the spatial resolution of their
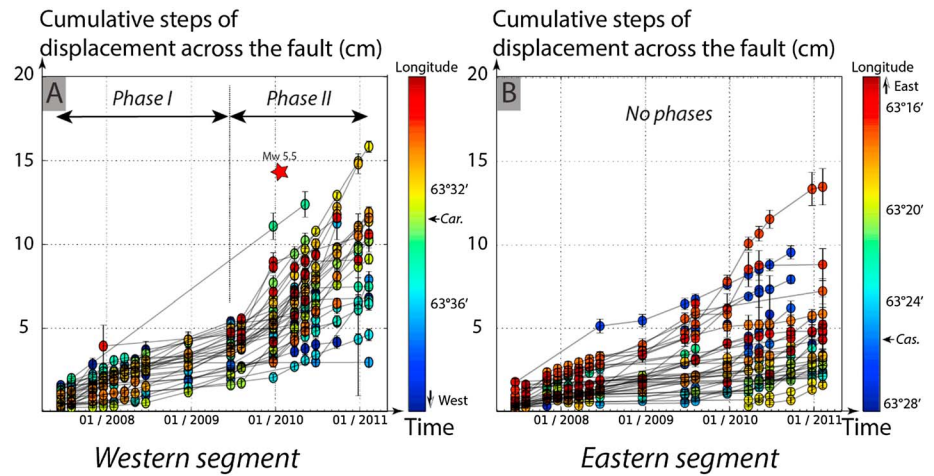
Figure 9. Cumulative displacement steps (in centimeters) across the El Pilar fault for each time step of the time series. Cumulative step estimation involves fitting the times series values weighted with RMS for each 480 m (or 16 pixels). For each estimation using 1, the standard deviation (error bars) is plotted. The dot color corresponds to the longitude along the fault. (a) Cumulative displacement steps (in centimeters) across the western segment. The average velocity of the two phases was defined using linear regression between cumulative displacement and the date at each longitude along the fault. Red star marks the M_W 5.5 earthquake in January 2010. (b) Cumulative displacement steps (in centimeters) across the eastern segment. X^2 value for each dot is plotted in Figure S9. Car., Cariaco and Cas., Casanay.

model was limited by the amount of available data. To improve the resolution, we carried out a similar inversion, but adding in our InSAR results. The GNSS velocity data used in the inversions result from three GNSS campaigns (2003–2005/2013) [*Reinoza et al.*, 2015]. For InSAR, the LOS mean velocities (2007–2011 period) from this study are used. LOS values are projected onto horizontal fault-parallel components (assuming no vertical displacement and only fault-parallel displacements as discussed in part 3) and are downsampled (weighted by RMS pixel values) at 400 m spacing and restricted to data points located in near field within 5 km of the El Pilar fault. We chose to restrict InSAR data coverage to a 10 km wide band around the El Pilar fault to mitigate possible longer wavelength residual orbital error or atmospheric perturbation, and because our data analysis had shown that most of the creep velocity jump signal across the fault was distributed within less than a few kilometers from the fault trace.

The slip distribution model was performed using the SDM software [*Wang et al.*, 2013a, 2013b], which has been successfully used to invert coseismic slip and afterslip [e.g., *Motagh et al.*, 2008, 2010; *Wang et al.*, 2009; *Diao et al.*, 2010, 2011; *Xu et al.*, 2010]. This inversion first performs a sensitivity-based iterative fitting approach; it calculates the portion of the data which can be explained per unit slip by a single patch. The slip distribution inversion uses an elastic half-space model [*Okada*, 1985] to calculate Green's function. To choose between the many possible slip models, the code chooses a slip model with an appropriate roughness in the slip distribution. Thus, the code solves a minimization problem applied to an objective function defined as

$$F(b) = ||Gb - y||^2 + \alpha^2 ||H\tau||^2 \qquad (2)$$

where G is the Green's function, b is the slip of subfaults, y is the ground observation, α is a positive smoothing factor, H is the finite difference approximation of the Laplacian operator multiplied by a weighting factor proportional to the slip amplitude, and τ represents the shear stress drop related to the slip distribution on the whole fault plane [*Wang et al.*, 2009].

We use a homogeneous Earth model with a Poisson ratio of 0.25 and a smoothing factor of 0.1 (see supporting information Figure S10). The fault is modeled by three vertical planes, with each plane segment separated into two parts: an upper part (0–20 km depth), which represents the seismogenic layer, and a lower part which represents the ductile layer. We considerably extended in depth and width the area of the model to avoid boundary effects. We considered only right-lateral slip (180° rake) on those planes. The upper part is discretized into square patches whose size is 1 km in length in the area covered by InSAR and 20 km elsewhere. The lower part is discretized into squares 10 km in length. The bend of Guarapiche (localized in Figure 7) is discretized separately. We fixed a threshold for the maximum of slip magnitude in the lower part
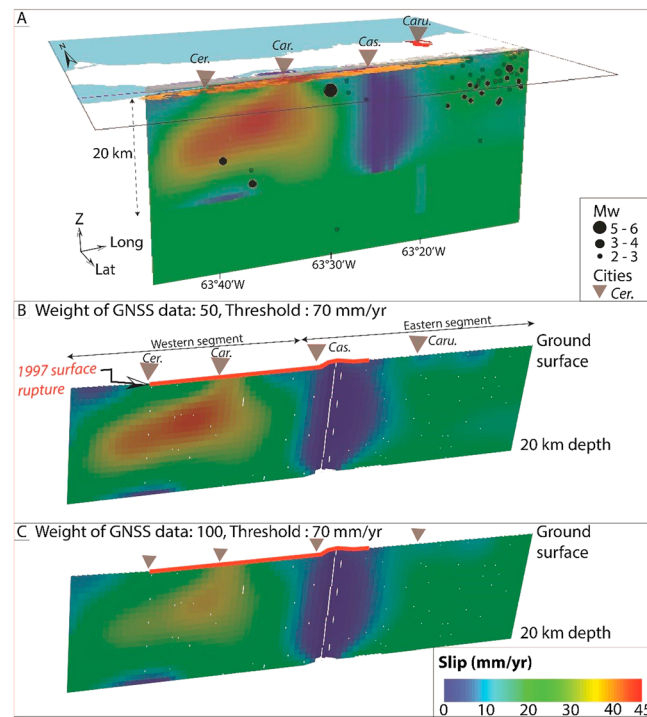
Figure 10. (a) Upper part 3-D view of western and eastern segments discretized for the slip distribution mode, with the seismicity recorded between 2007 and 2011 shown as black dots; the inversion displayed is the same than in Figure 10b. Slip distribution inversions performed with SDM. In these inversions, we used the LOS mean velocities measured during the 2007–2011 period (whole time span) and we remove the large wavelength from the InSAR data. (b) Slip distribution with a correlation of 95.20% for an inversion where GNSS data weight is 50 compared to InSAR data, and the slip magnitude cannot exceed 70 mm/yr. (c) Slip distribution with a correlation (or fit to the data) of 95.18% for an inversion where GNSS data have a weight of 100 compared to InSAR data, and the slip magnitude cannot exceed 70 mm/yr. Cer., Cerezal; Car., Cariaco; Cas., Casanay; and Caru., Carupano.

at 20 mm/yr in agreement with GPS far field velocities [*Pérez et al.*, 2001; *DeMets et al.*, 2010; *Jouanne et al.*, 2011; *Reinoza et al.*, 2015]. We also apply a threshold on the upper part of 70 mm/yr. We choose to use a relative weight for GNSS and InSAR data. The weight has been chosen in order to satisfy two criteria: allowing the model to reach long-term (geologic) slip rates below 20 km and to reduce residual errors for InSAR data. In order to invert velocities measured in 2007–2011 which is probably a transient event we give a low weight to the near field SMI1 station (0.01). Indeed, this station influence our inversion as the velocity estimated in 2003–2005–2013 represents an average fault behavior and not the transient behavior during the 2007–2011 period.

We tested several parameters in order to evaluate the robustness of coupled and uncoupled areas. For example, we tried several weightings for the GNSS and InSAR data, various slip magnitude thresholds (e.g., Figure 10), and change in dip for the upper dislocation (e.g., 65° northward, vertical, or 75° southward); we also tried using the InSAR data without first removing the large wavelength (the one shown in the supporting information Figure S6). The slip is not uniform in all our inversions, and the spatial distribution of slip is similar within ~5 km location uncertainty. For instance, in all inversions there is a zone between the western and eastern segments characterized by a slip rate lower than 3 mm/yr (Figure 10). Segmentation is also observed in all inversions: the western segment exhibits a widespread uncoupled area (characterized by a slip rate close to 30 mm/yr) reaching the surface, whereas the eastern segment slips at ~20 mm/yr. These patterns are in the same location in all the tests; thus, slip distribution inversions shown in Figure 10 are robust (see InSAR map of residuals in Figure 11 and simulated GNSS velocities in Figure S11). Our inversions show that during the ~3.5 year period, the aseismic slip (~17–18 mm/yr) released a moment of ~ 8.5×10^{17} N m which is equivalent to an earthquake of $M_w \sim 6.27$ (or M_w 6.25 for test C in Figure 10).

In addition, we inverted slip rates before and after the creep acceleration with the same method by keeping the same parameters and the same GNSS data (Figure 12). Slip distribution inversions show that the coupled zones are broadly at the same place during the two phases. These zones become smaller in Phase II (characterized by an increase of slip rate). These inversions are broadly consistent with cumulative displacement profiles across the fault (Figure 9), even if in the eastern segment profiles do not exactly match to the slip variation in the two inversions. Regarding residuals (shown in Figure S12), simulated GNSS velocities are similar to those of the first inversions (Figure S11); however, residuals for InSAR data are almost the double of the residuals in the slip distribution inversions of the velocities measured during the whole spanning interval (2007–2011). This difference is most important along the Guarapiche bend area in Phase II (Figure S11b).
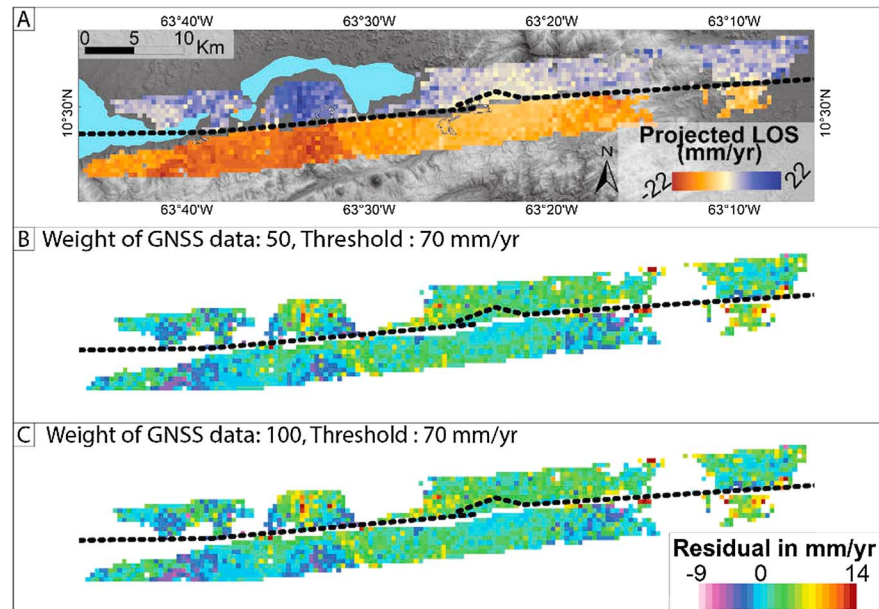
Figure 11. Map of residuals for three inversions. (a) InSAR velocity input. (b and c) Map of residuals for InSAR data for the two tests (displayed in Figures 10b and 10c). Simulated and observed GNSS velocities are displayed in Figure S11 in the supporting information.

6. Discussion

6.1. Short-Term Segmentation and Fault Properties

Detection of spatial variations in creep rate for the 2007–2011 period allows us to establish that two fault segments undergo different behavior. The shallow surface rate of the western segment reaches 25.3 ± 9.4 mm/yr on average (deduced from InSAR data) and has transient variations. On the contrary, slip in the eastern segment reaches 13.4 ± 6.9 mm/yr on average and does not present significant temporal variations. This segmentation observed in the short term (3.5 years) may not be persistent over longer timescales. For instance, it is possible that at other periods the western segment could return to a lower steady state value while the eastern segment could undergo acceleration. Nevertheless, GNSS campaigns (2003–2005–2013) show a consistent segmentation pattern (a western segment creeping faster than the eastern segment) [*Jouanne et al.*, 2011; *Reinoza et al.*, 2015].
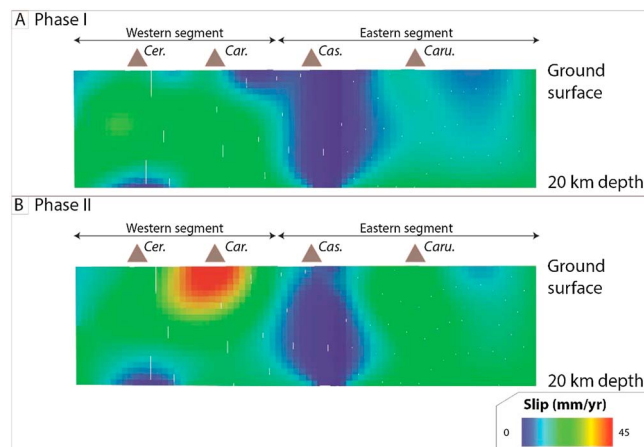

Figure 12. Slip distribution inversions before and after the acceleration (Phase I and Phase II in Figure 9). Inversions performed with SDM where GNSS data have a weight of 50 relative to InSAR data, and the slip magnitude cannot exceed 70 mm/yr. (a) Slip distribution inversions for InSAR velocities measured during the Phase I with a correlation of 91.50%. (b) Slip distribution inversions for InSAR velocities measured during the Phase II with a correlation of 90.82%. See residual map and simulated GNSS velocities in Figure S12. Cer., Cerezal; Car., Cariaco; Cas., Casanay; and Caru., Carupano.
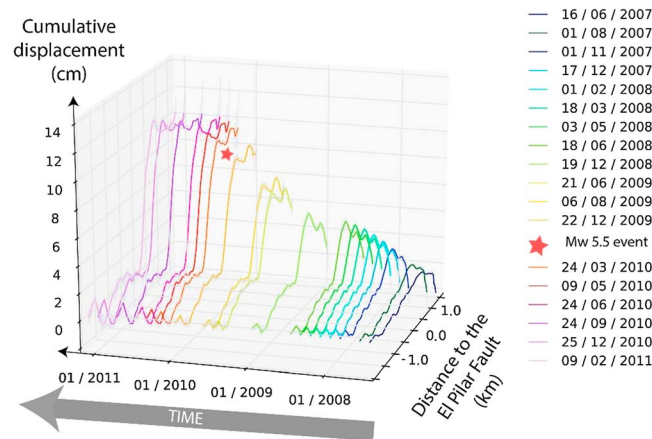
Figure 13. Profiles perpendicular to the fault showing smoothed cumulative displacement for each acquisition date (see Figure S13 in the supporting information for a version of this plot without smoothing). The profile crosses the fault at longitude 63°30'W, which is the location of the epicenter of the January 2010 M_w 5.5 earthquake (red star). Gray zones around curves correspond to the 1 sigma deviation.

Neotectonic analysis of geological markers shows evidence of fault geometry variations between the western and eastern creeping segments. As shown in Figure 7, the fault mapped in *Beltran et al.* [1996] is almost linear along the western segment, whereas the eastern segment is distributed along several parallel traces (e.g., bend of Guarapiche). Thus, the fault geometry could control the distribution of the creep as proposed by *Lindsey et al.* [2014] for the San Andreas fault.

Frictional properties could control the creep rate as predicted by the empirical law of the rate and state formalism [*Dieterich*, 1979; *Ruina*, 1983]. As the friction coefficient is related to the material characteristics surrounding the fault, there could be a lithological control on creep rate variations. Along the El Pilar fault, the presence of serpentine lenses, with quartzite and schist [*Vierbuchen*, 1984] along a fault plane characterized by an important creep (Figure 3), can be compared to experiments of shearing serpentinite ultramafic rocks juxtaposed against quartzite under hydrothermal conditions (200°–350°) carried out by *Moore and Lockner* [2013]. This experimental setup promotes aseismic slip at seismogenic depth more than serpentinite shearing experiments without quartzite rocks, and it also shows that long-term shearing of serpentinite against crustal rocks produces extremely weak minerals such as saponite and talc. Additionally, *Moore and Lockner* [2013] and *Scuderi et al.* [2015], among others suggest that faults can be characterized by strengthening and aseismic slip in the presence of high groundwater flow rates. This may be correlated to the existence of swamps near the western segment of the fault and also to the high number of hot springs and fumaroles [*Urbani*, 1989; *D'Amore et al.*, 1994; *López*, 2013]. Lastly, we note the concentration of microseismicity ($M_w < 2$) in the area where there are no serpentinite lenses at the surface (Figures 3 and 10). This concentration in the eastern segment could be due to a concentration of small asperities which are loaded by adjacent creep and cause failure. Presence of numerous asperities can be thus correlated to the lack of serpentines. Another explanation could be the variation in pore fluid which would reduce the effective normal stress and therefore the apparent coefficient of friction [*Gratier*, 2011; *Richard et al.*, 2014].

6.2. Link With Seismicity

Slip distribution models on the onshore segment of the El Pilar fault allow us to estimate that between 2007 and 2011 the slip released a moment of $8.0–8.5 \times 10^{17}$ N m, which corresponds to an earthquake of M_w ~6.26. Since moment released by the recorded seismicity during the same period of time is 1.55×10^{17} N m, the slip was mostly aseismic. This aseismic slip may control the distribution of microseismicity. Slip distribution models show that the microseismicity (M_w ~2) seems to occur in the transitional area between the uncoupled and coupled zones especially at the east (Figure 10a). In these areas, microseismicity could result from failure of asperities (coupled areas) loaded by adjacent creep in the surrounding uncoupled areas. The seismicity resulting from these failures is often linked to the creep rate [e.g., *Nadeau and McEvilly*, 2004] and can be defined as characteristically repeating earthquakes, although the waveforms and magnitudes of microseismic events would be needed to confirm this here.

Despite the low temporal resolution of InSAR analysis, it seems that there is no correlation between recorded seismicity and temporal slip rate variation (Figure 8). However, it should be noted that a M_w 5.5 event (January 2010), at the edge of the western segment, occurred after a period of creep rate acceleration. This may indicate that it was triggered by a rise in creep rate (Figure 13). A sequence of slow slip events followed by $M_w > 5$ earthquakes has been observed in subduction zones, where slow slip events probably induce abrupt stress changes and then earthquakes [e.g., *Radiguet et al.*, 2016]. However, this sequence is unusual along strike-slip

faults, and in fact, the opposite is often observed; for instance, along the San Andreas fault and the Haiyuan, M_w 4–5.5 events promote aseismic slip in the adjacent areas [e.g., *Murray and Segall*, 2005; *Taira et al.*, 2014].

At the regional scale, no significant seismic events were recorded in the vicinity of the El Pilar fault ($M_w > 4.5$) or in the neighboring countries ($M_w > 7$) [*International Seismological Centre*, 2013]. Therefore, local or remote earthquakes cannot explain the temporal creep variation that occurred in 2009. Slip distribution inversions from InSAR velocities measured before and after June 2009 show an increase of slip below Cariaco between the surface and 10 km depth (Figure 12). Changes in groundwater flow rates may explain this variation in the shallowest part (see section 6.1), especially as the western segment is close to swamp and hot springs. However, for the deepest part, the transient behavior could be explained by stress interactions with neighboring faults or by variation of friction properties [e.g., *Lienkaemper et al.*, 1997; *Scholz*, 1998; *Wei et al.*, 2013].

6.3. Aseismic Slip Types and Seismic Hazard

The 1997 event released a seismic moment of $M_o = 3.1 \times 10^{19}$ N m. The surface rupture was mapped in the field 2 days after the event over a distance of 30 km (Figures 14a and 14b). During this field investigation, the displacements measured yielded an average total slip ranging from ~20 cm to ~40 cm, assuming a crack-like rupture [*Pérez*, 1998; *Audemard*, 1999, 2006; *Baumbach et al.*, 2004]. Considering earthquake fault scaling laws of *Leonard* [2010] a seismic moment of $M_o = 3.1 \times 10^{19}$ N m corresponds to an average fault displacement of ~1.1 m. Therefore, only 20–35% of the expected displacement was accounted by the total "coseismic" slip observed. This discrepancy could be explained in part by the occurrence of off-fault deformation [*Zinke et al.*, 2014; *Milliner et al.*, 2016] or by aseismic slip (after the earthquake) on the shallow part of the fault as proposed in *Hussain et al.* [2016].

Actually, localized aseismic slip was detected in the field during the 6 years following the 1997 event (Figures 14a–14b). The total measured slip triples the surface coseismic slip and ranges from 50 to 120 cm [*Audemard*, 2006; *Jouanne et al.*, 2011], which is 50 to 100% of the expected average fault displacement corresponding to a M_w 6.9. This period of rapid slip after the earthquake is thus interpreted as an afterslip. Moreover, the logarithmic decay characterizing the afterslip phenomenon [*Marone et al.*, 1991; *Chang et al.*, 2013] has not been seen in the records from the 2003, 2005, and 2013 geodetic campaigns along the El Pilar fault segments (Figure 14a). This decay was also not detected by the temporal slip rate investigation between 2007 and 2011 carried out in this study; on the contrary, a rise in slip rate was observed. We can therefore hypothesize that short-term transient afterslip (during few years) may have been induced by the 1997 earthquake and it is over since 2002–2003.

In 2005 and 2013 two GNSS campaigns was carried out, considering stations ARI0-PER0 the El Pilar fault is creeping in average at 13 mm/yr. Between 2007 and 2011 the eastern segment showed a similar velocities (~13 mm/yr). However, in the western segment the creep is in average double (~26 mm/yr). This implies that the fault undergoes strong temporal variation to be in agreement with GNSS measurements. For example, along the western segment, between 2005 and 2007 and between 2012 and 2013 the creep rate had to decrease significantly (~0 mm/yr) to be in agreement with the 13 mm/yr deduced from GNSS measurements (Figure 14a). The El Pilar fault seems thus to be locked during several years and then undergoes transients of creep during several months. This transient behavior is also supported by the fact that the creep exceeds the plate relative velocity motion. This pattern was also observed in 2000–2003 in the western segment (markers b and d in Figure 14a). Several creeping fault around the world had a transient-like behavior: for example, the North Anatolian fault underwent a transient of 31 days [*Rousset et al.*, 2016] or the Haiyuan fault [*Jolivet et al.*, 2015b]. Moreover, along the 1999 Izmit surface rupture of the North Anatolian fault, *Hussain et al.* [2016] proposed that the steady state afterslip will probably undergo transient acceleration during the earthquake cycle. The installation of a creep meter will provide temporal coverage which could inform us about the duration creep events (i.e., several creep events during days or one creep event during several months).

Although it is not known if the El Pilar fault was creeping before 1997, 10 years after 1997 the aseismic slip is still high and undergoes accelerations. Thus, it is possible that the succession of locked and of large transients lasts during the interseismic period (before and after the 1997 events). To test this hypothesis, earthquake return periods can be evaluated for the cases with or without persistent creep and compared with available information about return period. For instance, considering a fully locked fault that is affected only by episodic
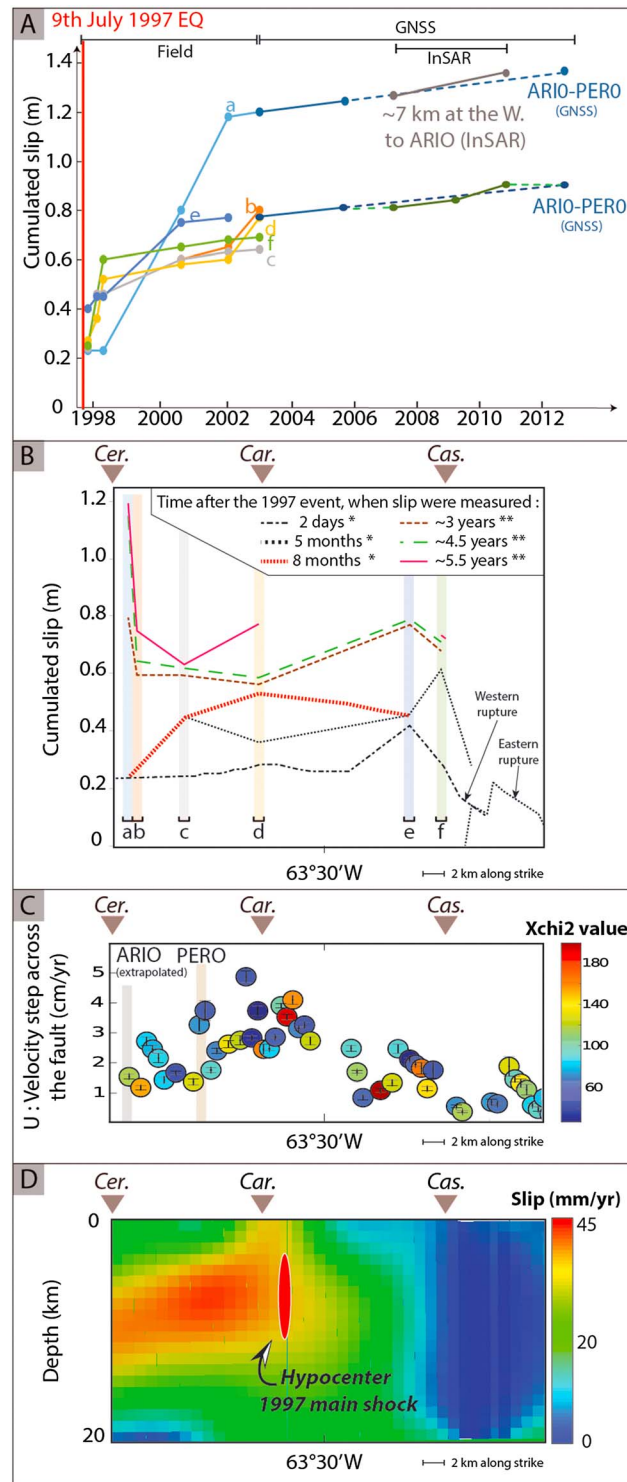
partial coupling due to transient aseismic afterslip during a short period of time (for example, less than 20 years) and a long-term slip rate of 20 mm/yr, the return period of a characteristic earthquake similar to the 1997 event (1 to 4 m of slip) would range from 50 to 200 years. However, assuming a stationary partial coupling of 12–13 mm/yr during the interseismic period, and a long-term slip rate of 20 mm/yr, the return period would increase from ~80 to 500 years. The latter case is more consistent with relevant paleoseismology studies which inferred return periods of ~ 400 years for large events [*Audemard*, 2006, 2011]. Thus, a short-term (several years) afterslip induced by an earthquake, succession of locked and of large transients during the interseismic period could better represent the seismic cycle of the El Pilar fault.

Considering that since 2003 the rapid afterslip decay has finished, we observe in Figures 14c and 14d the aseismic slip occurring during the earthquake cycle. We can thus propose that the coupled

Figure 14. Fault slip along the 1997 surface rupture. (a) Total slip measured after the 1997 event. Lines a, b, c, d, e, and f are localized in Figure 14b. These lines correspond to field measurements reported by *Audemard* [2006] and *Jouanne et al.* [2011]. Lines ARI0-PER0 display the total slip measured by GNSS between stations ARI0 and PER0 [*Reinoza et al.*, 2015]. (b) Field slip measurements along the 1997 surface rupture since 2–3 days after the 1997 event (Single asterisk and double asterisks signify that slip was measured in *Audemard* [2006] and *Jouanne et al.* [2011], respectively.) These measurements are the same than those plotted in Figure 14a. (c) InSAR velocity slip along the 1997 surface rupture (measured in this study from June 2007 to December 2011 in Figure 7). (d) Upper part of the slip distribution inversion performed in this study (see Figure 10). The figure displays the seismogenic layer until 20 km depth. The red area corresponds to the hypocenter of the 1997 event [*Baumbach et al.*, 2004, and references therein]. Figures 14b–14d are at the same scale (in longitude along the fault) and are located at the same localization (1997 surface rupture). Cer., City of Cerezal; Car., Cariaco; and Cas., Casanay.

area below Casanay corresponds to an asperity which may have been responsible for the 1997 earthquake (Figure 14d). At that time, the surrounding slipping areas could thus have been activated by the weakening dynamic triggered by the failure of this asperity. This could explain the existence of ground deformations (observed 2–3 days after the event) over a length exceeding the length of this asperity. Three months before the El Pilar 1997 event, a M_w 6.7 occurs in Tobago (~350 km from Casanay) [*Weber et al.*, 2015]. Despite this earthquake had a normal cinematic, it could have induced stress variation along the El Pilar which triggers the event.

Considering a long-term slip rate of 20 mm/yr and a seismogenic depth below the 1997 surface rupture (of 20 km), the slip deficit estimated from our model corresponds to an earthquake of M_w 5.1–5.5 (accounting for the seismic moment release due to seismicity over the 3.5 year period of observation). This implies that the fault accumulates strain and can release it during an earthquake. Therefore, to accumulate a slip deficit equivalent to the seismic moment of $M_o = 3.1 \times 10^{19}$ N m released during the 1997 event requires more than 800 years. This period is higher than the return period which confirms that we observe a large transient episode along the western segment.

Regarding seismic hazard, along the western segment, as we inferred increases and decreases in the slip rate over the 3.5 year study period, it would probably be necessary to perform a time-dependent seismic hazard forecast, as it has been proposed for the San Andreas fault [e.g., *Khoshmanesh et al.*, 2015] or for the Haiyuan fault [e.g., *Jolivet et al.*, 2015b]. The bend in the eastern segment, which has a constant and lower creep rate, has been considered a seismic barrier by *Audemard* [2006]. However, it could be interesting to perform an accurate seismic hazard evaluation, because this kind of fault can generate large seismic slips, as explained by *Noda and Lapusta* [2013]. Particular attention should also be paid to the transition area between these segments. Indeed, this zone seems to be coupled and able to provoke failures due to loading by adjacent creep, as it certainly happened in the case of the M_w 5.5 event.

7. Conclusion

In this paper, we use InSAR analyses in order to characterize the spatial and temporal variation of creep rate along the El Pilar fault. InSAR velocity profiles across the fault show a large step (greater than 2 mm/yr when projected into horizontal fault-parallel velocity), and demonstrate the continuity of creep localized along the El Pilar fault trace at the surface. Slip distribution inversions using GNSS velocities from three campaigns (2003–2005–2013) and the LOS mean velocities (estimated here on the 2007–2011 period) show that the aseismic slip releases a moment of ~ 8.0–8.5 × 10^{17} N m between the surface and 20 km depth during the 3.5 year observation period. Considering a long-term slip rate of 2 cm/yr, this implies that the fault accumulates strain (equivalent to a M_w 5.4–5.6 over 3.5 years) which can be released during an earthquake.

Analysis of the spatial variability of the creep rate between 2007 and 2011 allows us to distinguish two fault segments of the El Pilar fault which showed different behavior. The creep rate of the western segment reached 25.3 ± 9.4 mm/yr on average and underwent transient behavior. On the contrary, slip on the eastern segment reached 13.4 ± 6.9 mm/yr on average and did not show significant temporal creep variation. Locally, creep rates are higher than the relative plate motions which strongly suggest that it is a transient phenomenon. We investigated the geometrical and lithological characteristics which could explain this difference, and it appears that the faster creeping segment corresponds to a linear and unique trace which crosscuts a province containing quartzite and serpentinite. Future geodetic monitoring (ALOS-2, Sentinel SAR data) and installation of a permanent creep meter will further constrain the link between the fault geometry and lithology [e.g., *Thomas et al.*, 2014a].

Despite the relatively low temporal resolution (18 dates) of our study, the observation of transient behavior indicates that these segments were affected by episodic interseismic aseismic slip between 2007 and 2011. The rise in creep rate cannot be explained by a postseismic afterslip mechanism. The creep is thus interpreted as into interseimic creep showing transients.

References

Aguilar, I., C. Beck, F. Audemard, A.-L. Develle, M. Boussafir, C. Campos, and C. Crouzet (2016), Last millennium sedimentation in the Gulf of Cariaco (NE Venezuela): Evidence for morphological changes of gulf entrance and possible relations with large earthquakes, *Comptes Rendus Geosci.*, *348*(1), 70–79, doi:10.1016/j.crte.2015.10.001.

Alsdorf, D. E., J. M. Melack, T. Dunne, L. A. K. Mertes, L. L. Hess, and L. C. Smith (2000), Interferometric radar measurements of water level changes on the Amazon flood plain, *Nature*, *404*(6774), 174–177, doi:10.1038/35004560.

Altez, R., and F. Audemard (2008), El sismo de 1629 en cumaná: Aportes para una nueva historia sísmica del oriente venezolano, *Bol. Téc. IMME*, *46*(2), 53–71.

Audemard, F. (2006), Surface rupture of the Cariaco July 09, 1997 earthquake on the El Pilar fault, northeastern Venezuela, *Tectonophysics*, *424*(1–2), 19–39, doi:10.1016/j.tecto.2006.04.018.

Audemard, F. (2007), Revised seismic history of the El Pilar fault, northeastern Venezuela, from the Cariaco 1997 earthquake and recent preliminary paleoseismic results, *J. Seismol.*, *11*(3), 311–326, doi:10.1007/s10950-007-9054-2.

Audemard, F. (2009), Key issues on the post-Mesozoic Southern Caribbean Plate boundary, *Geol. Soc. Lond. Spec. Publ.*, *328*(1), 569–586, doi:10.1144/SP328.23.

Audemard, F. (2011), Multiple-trench investigations across the newly ruptured segment of the El Pilar fault in northeastern Venezuela after the 1997 Cariaco earthquake, *Geol. Soc. Am. Spec. Pap.*, *479*, 133–157, doi:10.1130/2011.2479(06).

Audemard, F. A. (1999), El sismo de Cariaco del 09 de julio de 1997, edo. Sucre, Venezuela: Nucleación y progresión de la ruptura a partir de observaciones geológicas, *Mem VI Cong Venez Sismol. E Ing. Sísmica*.

Audemard, F. E., and F. Audemard (2002), Structure of Merida Andes, Venezuela: Relations with South America-Caribbean geodynamic interaction, *Tectonophysics*, *345*, 299–327.

Audemard, F., M. N. Machette, J. W. Cox, R. L. Dart, and K. M. Haller (2000), Map and database of Quaternary faults in Venezuela and its offshore regions—Scale 1:2 000 000. Acompañado por noticia explicativa: Map and Database of Quaternary Faults in Venezuela and Offshore regions (USGS Open-File Report 00-18, 78 p). A project of the International Lithosphere Program Task Group II-2: Major active faults of the world (Regional Coord.: Carlos Costa, Univ. San Luis-Argentina, ILP II-2 co-chairman Western Hemisphere: Michael Machette, USGS-Colorado), *USGS Numbered Series*, *2000-18*, 78 p.

Avouac, J.-P. (2015), From geodetic imaging of seismic and aseismic fault slip to dynamic modeling of the seismic cycle, *Annu. Rev. Earth Planet. Sci.*, *43*(1), 233–271, doi:10.1146/annurev-earth-060614-105302.

Barbot, S., P. Agram, and M. De Michele (2013), Change of apparent segmentation of the San Andreas fault around Parkfield from space geodetic observations across multiple periods, *J. Geophys. Res. Solid Earth*, *118*, 6311–6327, doi:10.1002/2013JB010442.

Baumbach, M., H. Grosser, G. R. Torres, J. L. R. Gonzales, M. Sobiesiak, and W. Welle (2004), Aftershock pattern of the July 9, 1997 $M_w = 6.9$ Cariaco earthquake in northeastern Venezuela, *Tectonophysics*, *379*(1–4), 1–23, doi:10.1016/j.tecto.2003.10.018.

Beltran, C. (1993), Neotectonic map of Venezuela, scale 1: 2 000 000, *Venezuelan Found. Seismol. Res. FUNVISIS*.

Beltran, C., A. Singer, and J. A. Rodriguez (1996), The El Pilar Fault active trace (northeastern Venezuela): Neotectonic evidences and paleoseismic data, in *3rd Symposium International sur la Géodynamique Andine, Saint-Malo, France*, pp. 153–156, ORSTOM, Paris.

Blanpied, M. L., D. A. Lockner, and J. D. Byerlee (1991), Fault stability inferred from granite sliding experiments at hydrothermal conditions, *Geophys. Res. Lett.*, *18*(4), 609–612, doi:10.1029/91GL00469.

Çakir, Z., J.-B. de Chabalier, R. Armijo, B. Meyer, A. Barka, and G. Peltzer (2003), Coseismic and early post-seismic slip associated with the 1999 Izmit earthquake (Turkey), from SAR interferometry and tectonic field observations, *Geophys. J. Int.*, *155*(1), 93–110, doi:10.1046/j.1365-246X.2003.02001.x.

Cavalié, O., C. Lasserre, M.-P. Doin, G. Peltzer, J. Sun, X. Xu, and Z.-K. Shen (2008), Measurement of interseismic strain across the Haiyuan fault (Gansu, China), by InSAR, *Earth Planet. Sci. Lett.*, *275*(3–4), 246–257, doi:10.1016/j.epsl.2008.07.057.

Cetin, E., Z. Cakir, M. Meghraoui, S. Ergintav, and A. M. Akoglu (2014), Extent and distribution of aseismic slip on the Ismetpaşa segment of the North Anatolian fault (Turkey) from persistent scatterer InSAR, *Geochem. Geophys. Geosyst.*, *15*, 2883–2894, doi:10.1002/2014GC005307.

Champenois, J., B. Fruneau, E. Pathier, B. Deffontaines, K.-C. Lin, and J.-C. Hu (2012), Monitoring of active tectonic deformations in the Longitudinal Valley (Eastern Taiwan) using persistent scatterer InSAR method with ALOS PALSAR data, *Earth Planet. Sci. Lett.*, *337–338*, 144–155, doi:10.1016/j.epsl.2012.05.025.

Chang, S.-H., J.-P. Avouac, S. Barbot, and J.-C. Lee (2013), Spatially variable fault friction derived from dynamic modeling of aseismic afterslip due to the 2004 Parkfield earthquake, *J. Geophys. Res. Solid Earth*, *118*, 3431–3447, doi:10.1002/jgrb.50231.

Chaussard, E., F. Amelung, H. Abidin, and S.-H. Hong (2013), Sinking cities in Indonesia: ALOS PALSAR detects rapid subsidence due to groundwater and gas extraction, *Remote Sens. Environ.*, *128*, 150–161, doi:10.1016/j.rse.2012.10.015.

Chaussard, E., R. Bürgmann, H. Fattahi, C. W. Johnson, R. Nadeau, T. Taira, and I. Johanson (2015a), Interseismic coupling and refined earthquake potential on the Hayward-Calaveras fault zone, *J. Geophys. Res. Solid Earth*, *120*, 8570–8590, doi:10.1002/2015JB012230.

Chaussard, E., R. Bürgmann, H. Fattahi, R. M. Nadeau, T. Taira, C. W. Johnson, and I. Johanson (2015b), Potential for larger earthquakes in the East San Francisco Bay Area due to the direct connection between the Hayward and Calaveras faults, *Geophys. Res. Lett.*, *42*, 2734–2741, doi:10.1002/2015GL063575.

Clark, S. A., C. A. Zelt, M. B. Magnani, and A. Levander (2008), Characterizing the Caribbean-South American plate boundary at 64°W using wide-angle seismic data, *J. Geophys. Res.*, *113*, B07401, doi:10.1029/2007JB005329.

D'Amore, F., G. Gianelli, and E. Corazza (1994), The geothermal area of El Pilar-Casanay, state of sucre, Venezuela. Geochemical exploration and model, *Geothermics*, *23*(3), 283–304, doi:10.1016/0375-6505(94)90005-1.

de Juana, C. G., J. M. I. de Arozena, and X. P. Cadillat (1980), *Geología de Venezuela y de sus Cuencas Petrolíferas*, Foninves, Venezuela.

DeMets, C., R. G. Gordon, and D. F. Argus (2010), Geologically current plate motions, *Geophys. J. Int.*, *181*(1), 1–80, doi:10.1111/j.1365-246X.2009.04491.x.

Diao, F., X. Xiong, R. Wang, Y. Zheng, and H. Hsu (2010), Slip model of the 2008 M_w 7.9 Wenchuan (China) earthquake derived from co-seismic GPS data, *Earth Planets Space*, *62*, 869–874, doi:10.5047/eps.2009.05.003.

Diao, F., X. Xiong, and R. Wang (2011), Mechanisms of transient postseismic deformation following the 2001 M_w 7.8 Kunlun (China) earthquake, *Pure Appl. Geophys.*, *168*, 767–779, doi:10.1007/s00024-010-0154-5.

Dieterich, J. H. (1979), Modeling of rock friction: 1. Experimental results and constitutive equations, *J. Geophys. Res.*, *84*(B5), 2161–2168, doi:10.1029/JB084iB05p02161.

Doin, M. P., C. Lasserre, G. Peltzer, O. Cavalié, and C. Doubre (2009), Corrections of stratified tropospheric delays in SAR interferometry: Validation with global atmospheric models, *J. Appl. Geophys.*, *69*(1), 35–50, doi:10.1016/j.jappgeo.2009.03.010.

Doin, M. P., F. Lodge, S. Guillaso, R. Jolivet, C. Lasserre, G. Ducret, R. Grandin, E. Pathier, and V. Pinel (2011), Presentation of the small baseline NSBAS processing chain on a case example: The Etna deformation monitoring from 2003 to 2010 using ENVISAT data, in *Proceedings of the Fringe symposium, Frascati, Italy*, ESA SP-697.

Doin, M.-P., C. Twardzik, G. Ducret, C. Lasserre, S. Guillaso, and S. Jianbao (2015), InSAR measurement of the deformation around Siling Co Lake: Inferences on the lower crust viscosity in central Tibet, *J. Geophys. Res. Solid Earth*, *120*, 5290–5310, doi:10.1002/2014JB011768.

Ducret, G., M.-P. Doin, R. Grandin, C. Lasserre, and S. Guillaso (2014), DEM corrections before unwrapping in a small baseline strategy for InSAR time series analysis, *IEEE Geosci. Remote Sens. Lett.*, *11*(3), 696–700, doi:10.1109/LGRS.2013.2276040.

Fajardo, A. (2015), Neotectonic evolution of the Serrania Del Interior range and Monagas fold and thrust belt, Eastern Venezuela: Morphotectonics, seismic profiles analyses and paleomagnetism, PhD thesis, Université de Pau et des Pays de l'Adour, France.

FUNVISIS (1994), Estudio neotectonico y de geologia de fallas activas de la region Nororiental de Venezuela, Proyecto Intevep, Technical report.

FUNVISIS (2010), Reporte de mecanismo focal obtenido con información de polaridad para primera llegad -onda P-, determinada en cada estación sismológica involucrada en el analisis, Technical online report. [Available at http://www.funvisis.gob.ve/mecanismos_focales.php?pag=4.]

Goldstein, R., H. Zebker, and C. Werner (1988), Satellite radar interferometry—Two-dimensional phase unwrapping, *Radio Sci.*, *23*(4), 713–720, doi:10.1029/RS023i004p00713.

Grandin, R., M.-P. Doin, L. Bollinger, B. Pinel-Puysségur, G. Ducret, R. Jolivet, and S. N. Sapkota (2012), Long-term growth of the Himalaya inferred from interseismic InSAR measurement, *Geology*, *40*(12), 1059–1062, doi:10.1130/G33154.1.

Gratier, J.-P. (2011), Fault permeability and strength evolution related to fracturing and healing episodic processes (years to millennia): The role of pressure solution, *Oil Gas Sci. Technol. Rev. D'IFP Energy Nouv.*, *66*(3), 491–506, doi:10.2516/ogst/2010014.

Gratier, J.-P., J. Richard, F. Renard, S. Mittempergher, M.-L. Doan, G. D. Toro, J. Hadizadeh, and A.-M. Boullier (2011), Aseismic sliding of active faults by pressure solution creep: Evidence from the San Andreas fault observatory at depth, *Geology*, *39*(12), 1131–1134, doi:10.1130/G32073.1.

Hackley, P. C., F. Urbani, A. W. Karlsen, and C. P. Garrity (2005), Geologic shaded relief map of Venezuela, U.S. Geological Survey Open File Report, 1038.

Hernandez, G., T. Rossi, J. Stephan, and R. Blanchet (1987), Etude géologique de la Serrania del Interior Oriental (Venezuela) sur le transect Cariaco-Maturin, *Rev. Inst. Fr. Pétrole*, *42*(1), 3–30.

Hussain, E., T. J. Wright, R. J. Walters, D. Bekaert, A. Hooper, and G. A. Houseman (2016), Geodetic observations of postseismic creep in the decade after the 1999 Izmit earthquake, Turkey: Implications for a shallow slip deficit, *J. Geophys. Res. Solid Earth*, *121*, 2980–3001, doi:10.1002/2015JB012737.

International Seismological Centre (2013), *On-line Bulletin*, Int. Seis. Cent, Thatcham, U. K.

Jacome, M., N. Kusznir, and S. Flint (1999), Structural and isostatic modelling of Serranía del Interior thrust belt and Monagas foreland basin: Eastern Venezuela, in *Fourth International Symposium on Andean Geodynamics Göttingen* (*Germany*), Oct, pp. 4–6.

Jolivet, R., R. Grandin, C. Lasserre, M.-P. Doin, and G. Peltzer (2011), Systematic InSAR tropospheric phase delay corrections from global meteorological reanalysis data, *Geophys. Res. Lett.*, *38*, L17311, doi:10.1029/2011GL048757.

Jolivet, R., C. Lasserre, M.-P. Doin, S. Guillaso, G. Peltzer, R. Dailu, J. Sun, Z.-K. Shen, and X. Xu (2012), Shallow creep on the Haiyuan fault (Gansu, China) revealed by SAR interferometry, *J. Geophys. Res.*, *117*, B06401, doi:10.1029/2011JB008732.

Jolivet, R., C. Lasserre, M.-P. Doin, G. Peltzer, J.-P. Avouac, J. Sun, and R. Dailu (2013), Spatio-temporal evolution of aseismic slip along the Haiyuan fault, China: Implications for fault frictional properties, *Earth Planet. Sci. Lett.*, *377–378*, 23–33, doi:10.1016/j.epsl.2013.07.020.

Jolivet, R., M. Simons, P. S. Agram, Z. Duputel, and Z.-K. Shen (2015a), Aseismic slip and seismogenic coupling along the central San Andreas fault, *Geophys. Res. Lett.*, *42*, 297–306, doi:10.1002/2014GL062222.

Jolivet, R., T. Candela, C. Lasserre, F. Renard, Y. Klinger, and M.-P. Doin (2015b), The burst-like behavior of aseismic slip on a rough fault: The creeping section of the Haiyuan fault, China, *Bull. Seismol. Soc. Am.*, *105*(1), 480–488, doi:10.1785/0120140237.

Jouanne, F., F. A. Audemard, C. Beck, A. Van Welden, R. Ollarves, and C. Reinoza (2011), Present-day deformation along the El Pilar fault in eastern Venezuela: Evidence of creep along a major transform boundary, *J. Geodyn.*, *51*(5), 398–410, doi:10.1016/j.jog.2010.11.003.

Kaneko, Y., Y. Fialko, D. T. Sandwell, X. Tong, and M. Furuya (2013), Interseismic deformation and creep along the central section of the North Anatolian fault (Turkey): InSAR observations and implications for rate-and-state friction properties, *J. Geophys. Res. Solid Earth*, *118*, 316–331, doi:10.1029/2012JB009661.

Khoshmanesh, M., M. Shirzaei, and R. M. Nadeau (2015), Time-dependent model of aseismic slip on the central San Andreas fault from InSAR time series and repeating earthquakes, *J. Geophys. Res. Solid Earth*, *120*, 6658–6679, doi:10.1002/2015JB012039.

Kim, J.-W., Z. Lu, H. Lee, C. K. Shum, C. M. Swarzenski, T. W. Doyle, and S.-H. Baek (2009), Integrated analysis of PALSAR/Radarsat-1 InSAR and ENVISAT altimeter data for mapping of absolute water level changes in Louisiana wetlands, *Remote Sens. Environ.*, *113*(11), 2356–2365, doi:10.1016/j.rse.2009.06.014.

Larson, K. M., A. R. Lowry, V. Kostoglodov, W. Hutton, O. Sánchez, K. Hudnut, and G. Suárez (2004), Crustal deformation measurements in Guerrero, Mexico, *J. Geophys. Res.*, *109*, B04409, doi:10.1029/2003JB002843.

Leonard, M. (2010), Earthquake fault scaling: Self-consistent relating of rupture length, width, average displacement, and moment release, *Bull. Seismol. Soc. Am.*, *100*(5A), 1971–1988, doi:10.1785/0120090189.

Levenberg, K. (1944), A method for the solution of certain problems in least squares, *Q. Appl. Math.*, *2*, 164–168.

Lienkaemper, J. J., J. S. Galehouse, and R. W. Simpson (1997), Creep response of the Hayward fault to stress changes caused by the Loma Prieta earthquake, *Science*, *276*(5321), 2014–2016, doi:10.1126/science.276.5321.2014.

Lindsey, E. O., Y. Fialko, Y. Bock, D. T. Sandwell, and R. Bilham (2014), Localized and distributed creep along the southern San Andreas fault, *J. Geophys. Res. Solid Earth*, *119*, 7909–7922, doi:10.1002/2014JB011275.

López, L. V. H. (2013), Hidrogeoquímica de aguas termales de las zonas de El Pilar y Los Ipures, Estado Sucre, Venezuela, Thesis de grado de Licencia, Universidad de Oriente Núcleo de Sucre., 31 January.

López-Quiroz, P., M.-P. Doin, F. Tupin, P. Briole, and J.-M. Nicolas (2009), Time series analysis of Mexico City subsidence constrained by radar interferometry, *J. Appl. Geophys.*, *69*(1), 1–15, doi:10.1016/j.jappgeo.2009.02.006.

Marone, C. J., C. H. Scholtz, and R. Bilham (1991), On the mechanics of earthquake afterslip, *J. Geophys. Res.*, *96*(B5), 8441–8452, doi:10.1029/91JB00275.

Marquardt, D. (1963), An algorithm for least-squares estimation of nonlinear parameters, *J. Soc. Ind. Appl. Math.*, *11*(2), 431–441, doi:10.1137/0111030.

Metz, H. L. (1965), Geology of the El Pilar fault zone state of Sucre, Venezuela, in *IV Caribbean Geological Conference*, pp. 293–298, Mobil Oil Company, Trinidad.

Milliner, C. W. D., C. Sammis, A. A. Allam, J. F. Dolan, J. Hollingsworth, S. Leprince, and F. Ayoub (2016), Resolving fine-scale heterogeneity of co-seismic slip and the relation to fault structure, *Sci. Rep.*, *6*, 27201, doi:10.1038/srep27201.

Moore, D. E., and D. A. Lockner (2013), Chemical controls on fault behavior: Weakening of serpentinite sheared against quartz-bearing rocks and its significance for fault creep in the San Andreas system, *J. Geophys. Res. Solid Earth*, *118*, 2558–2570, doi:10.1002/jgrb.50140.

Motagh, M., R. Wang, T. R. Walter, R. Buergmann, E. Fielding, J. Anderssohn, and J. Zschau (2008), Coseismic slip model of the 2007 August Pisco earthquake (Peru) as constrained by wide swath radar observations, *Geophys. J. Int.*, *174*(3), 842–848, doi:10.1111/j.1365-246X.2008.03852.x.

Motagh, M., B. Schurr, J. Anderssohn, B. Cailleau, T. R. Walter, R. Wang, and J.-P. Villotte (2010), Subduction earthquake deformation associated with 14 November 2007, M_w 7.8 Tocopilla earthquake in Chile: Results from InSAR and aftershocks, *Tectonophysics*, *490*(1–2), 60–68, doi:10.1016/j.tecto.2010.04.033.

Murray, J. R., and P. Segall (2005), Spatiotemporal evolution of a transient slip event on the San Andreas fault near Parkfield, California, *J. Geophys. Res.*, *110*, B09407, doi:10.1029/2005JB003651.

Nadeau, R. M., and T. V. McEvilly (2004), Periodic pulsing of characteristic microearthquakes on the San Andreas fault, *Science*, *303*(5655), 220–222.

Noda, H., and N. Lapusta (2013), Stable creeping fault segments can become destructive as a result of dynamic weakening, *Nature*, *493*(7433), 518–521, doi:10.1038/nature11703.

Okada, Y. (1985), Surface deformation due to shear and tensile faults in a half-space, *Bull. Seismol. Soc. Am.*, *75*(4), 1135–1154.

Pérez, O. J. (1998), Seismological report on the $M_w = 6.8$ strong shock of 9 July 1997 in Cariaco, northeastern Venezuela, *Bull. Seismol. Soc. Am.*, *88*(3), 874–879.

Pérez, O. J., and Y. P. Aggarwal (1981), Present-day tectonics of the southeastern Caribbean and northeastern Venezuela, *J. Geophys. Res.*, *86*(B11), 10,791–10,804, doi:10.1029/JB086iB11p10791.

Pérez, O. J., R. Bilham, R. Bendick, J. R. Velandia, N. Hernández, C. Moncayo, M. Hoyer, and M. Kozuch (2001), Velocity field across the southern Caribbean plate boundary and estimates of Caribbean/South-American plate motion using GPS geodesy 1994–2000, *Geophys. Res. Lett.*, *28*(15), 2987–2990, doi:10.1029/2001GL013183.

Pindell, J., L. Kennan, G. Draper, W. Maresch, and K. Stanek (2006), Foundations of Gulf of Mexico and Caribbean evolution: Eight controversies resolved, *Geol. Acta Int. Earth Sci. J.*, *4*(1), 303–341.

Rabus, B., M. Eineder, A. Roth, and R. Bamler (2003), The Shuttle Radar Topography Mission—A new class of digital elevation models acquired by spaceborne radar, *ISPRS J. Photogramm. Remote Sens.*, *57*(4), 241–262, doi:10.1016/S0924-2716(02)00124-7.

Radiguet, M., H. Perfettini, N. Cotte, A. Gualandi, B. Valette, V. Kostoglodov, T. Lhomme, A. Walpersdorf, E. Cabral Cano, and M. Campillo (2016), Triggering of the 2014 M_w7.3 Papanoa earthquake by a slow slip event in Guerrero, Mexico, *Nat. Geosci.*, doi:10.1038/ngeo2817.

Reinoza, C. E. (2014), Application de la géodésie satellitaire GNSS à haute résolution à la déformation de la marge Sud-Caraïbe. Implication pour l'aléa sismique dans l'Ouest et le Nord-Est du Venezuela., PhD thesis, Université Joseph Fourier/Université de Savoie Mont-Blanc, Chambéry, 15 December.

Reinoza, C. E., F. Jouanne, F. Audemard, M. Schmitz, and C. Beck (2015), Geodetic exploration of strain along the El Pilar fault in northeastern Venezuela, *J. Geophys. Res. Solid Earth*, *120*, 1993–2013, doi:10.1002/2014JB011483.

Richard, J., J.-P. Gratier, M.-L. Doan, A.-M. Boullier, and F. Renard (2014), Rock and mineral transformations in a fault zone leading to permanent creep: Interactions between brittle and viscous mechanisms in the San Andreas fault, *J. Geophys. Res. Solid Earth*, *119*, 8132–8153, doi:10.1002/2014JB011489.

Rosen, P. A., S. Hensley, G. Peltzer, and M. Simons (2004), Updated repeat orbit interferometry package released, *Eos Trans. Am. Geophys. Union*, *85*(5), 47–47, doi:10.1029/2004EO050004.

Rousset, B., R. Jolivet, M. Simons, C. Lasserre, B. Riel, P. Milillo, Z. Çakir, and F. Renard (2016), An aseismic slip transient on the North Anatolian fault, *Geophys. Res. Lett.*, *43*, 3254–3262, doi:10.1002/2016GL068250.

Ruina, A. (1983), Slip instability and state variable friction laws, *J. Geophys. Res.*, *88*(B12), 10,359–10,370, doi:10.1029/JB088iB12p10359.

Ryan, W. B. F., et al. (2009), Global multi-resolution topography synthesis, *Geochem. Geophys. Geosyst.*, *10*, Q03014, doi:10.1029/2008GC002332.

Ryder, I., and R. Bürgmann (2008), Spatial variations in slip deficit on the central San Andreas fault from InSAR, *Geophys. J. Int.*, *175*(3), 837–852, doi:10.1111/j.1365-246X.2008.03938.x.

Schmidt, D. A., R. Bürgmann, R. M. Nadeau, and M. d'Alessio (2005), Distribution of aseismic slip rate on the Hayward fault inferred from seismic and geodetic data, *J. Geophys. Res.*, *110*, B08406, doi:10.1029/2004JB003397.

Scholz, C. H. (1998), Earthquakes and friction laws, *Nature*, *391*(6662), 37–42, doi:10.1038/34097.

Scuderi, M. M., B. M. Carpenter, P. A. Johnson, and C. Marone (2015), Poromechanics of stick-slip frictional sliding and strength recovery on tectonic faults, *J. Geophys. Res. Solid Earth*, *120*, 6895–6912, doi:10.1002/2015JB011983.

Shirzaei, M., and R. Bürgmann (2013), Time-dependent model of creep on the Hayward fault from joint inversion of 18 years of InSAR and surface creep data, *J. Geophys. Res. Solid Earth*, *118*, 1733–1746, doi:10.1002/jgrb.50149.

Shirzaei, M., R. Bürgmann, and T. Taira (2013), Implications of recent asperity failures and aseismic creep for time-dependent earthquake hazard on the Hayward fault, *Earth Planet. Sci. Lett.*, *371–372*, 59–66, doi:10.1016/j.epsl.2013.04.024.

Taira, T., R. Bürgmann, R. M. Nadeau, and D. S. Dreger (2014), Variability of fault slip behavior along the San Andreas fault in the San Juan Bautista Region, *J. Geophys. Res. Solid Earth*, *119*, 8827–8844, doi:10.1002/2014JB011427.

Thatcher, W. (1979), Systematic inversion of geodetic data in central California, *J. Geophys. Res.*, *84*(B5), 2283–2295, doi:10.1029/JB084iB05p02283.

Thomas, M. Y., J.-P. Avouac, and J.-C. Lee (2014a), Lithological control on the deformation mechanism and the mode of fault slip on the Longitudinal Valley fault, Taiwan, *Tectonophysics*, *632*, 48–63, doi:10.1016/j.tecto.2014.05.038.

Thomas, M. Y., J.-P. Avouac, J. Champenois, J.-C. Lee, and L.-C. Kuo (2014b), Spatio-temporal evolution of seismic and aseismic slip on the Longitudinal Valley fault, Taiwan, *J. Geophys. Res. Solid Earth*, *119*, 5114–5139, doi:10.1002/2013JB010603.

Turner, R. C., M. Shirzaei, R. M. Nadeau, and R. Bürgmann (2015), Slow and Go: Pulsing slip rates on the creeping section of the San Andreas fault, *J. Geophys. Res. Solid Earth*, *120*, 5940–5951, doi:10.1002/2015JB011998.

Urbani, F. (1989), Geothermal reconnaissance of northeastern Venezuela, *Geothermics*, *18*(3), 403–427, doi:10.1016/0375-6505(89)90066-7.

Van Daele, M., et al. (2011), Reconstruction of Late-Quaternary sea- and lake-level changes in a tectonically active marginal basin using seismic stratigraphy: The Gulf of Cariaco, NE Venezuela, *Mar. Geol.*, *279*(1–4), 37–51, doi:10.1016/j.margeo.2010.10.011.

Vierbuchen, R. (1984), The geology of the El-Pilar fault zone and adjacent areas in northeastern Venezuela, *Geol. Soc. Am. Mem.*, *162*, 189–212.

Vignali, M. (1977), Geology between Casanay and El Pilar (El Pilar fault zone), Estado Sucre, Venezuela, in *VIIIth Caribb. Geol. Conf.*, *Curaçao*, pp. 215–216.

Wang, L., R. Wang, F. Roth, B. Enescu, S. Hainzl, and S. Ergintav (2009), Afterslip and viscoelastic relaxation following the 1999 *M* 7.4 İzmit earthquake from GPS measurements, *Geophys. J. Int.*, *178*(3), 1220–1237, doi:10.1111/j.1365-246X.2009.04228.x.

Wang, R., F. Diao, and A. Hoechner (2013a), SDM—A geodetic inversion code incorporating with layered crust structure and curved fault geometry, in *EGU General Assembly Conference Abstracts*, vol. 15, p. EGU2013.

Wang, R., S. Parolai, M. Ge, M. Jin, T. R. Walter, and J. Zschau (2013b), The 2011 M_w 9.0 Tohoku earthquake: Comparison of GPS and strong-motion data, *Bull. Seismol. Soc. Am.*, *103*, 1336–1347, doi:10.1785/0120110264.

Weber, J. C., T. H. Dixon, C. DeMets, W. B. Ambeh, P. Jansma, G. Mattioli, J. Saleh, G. Sella, R. Bilham, and O. Pérez (2001), GPS estimate of relative motion between the Caribbean and South American plates, and geologic implications for Trinidad and Venezuela, *Geology*, *29*(1), 75–78, doi:10.1130/0091-7613(2001)029<0075:GEORMB>2.0.CO;2.

Weber, J. C., H. Geirsson, J. L. Latchman, K. Shaw, P. La Femina, S. Wdowinski, M. Higgins, C. Churches, and E. Norabuena (2015), Tectonic inversion in the Caribbean–South American plate boundary: GPS geodesy, seismology, and tectonics of the M-w 6.7 22 April 1997 Tobago earthquake, *Tectonics*, *34*, 1181–1194, doi:10.1002/2014TC003665.

Wei, M., and D. T. Sandwell (2010), Decorrelation of L-Band and C-Band interferometry over vegetated areas in California, *IEEE Trans. Geosci. Remote Sens.*, *48*(7), 2942–2952, doi:10.1109/TGRS.2010.2043442.

Wei, M., D. Sandwell, and Y. Fialko (2009), A silent M_w 4.7 slip event of October 2006 on the Superstition Hills fault, southern California, *J. Geophys. Res.*, *114*, B07402, doi:10.1029/2008JB006135.

Wei, M., Y. Kaneko, Y. Liu, and J. J. McGuire (2013), Episodic fault creep events in California controlled by shallow frictional heterogeneity, *Nat. Geosci.*, *6*(7), 566–570, doi:10.1038/ngeo1835.

Xu, C., Y. Liu, Y. Wen, and R. Wang (2010), Coseismic slip distribution of the 2008 M_w 7.9 Wenchuan earthquake from joint inversion of GPS and InSAR data, *Bull. Seismol. Soc. Am.*, *100*(5B), 2736–2749, doi:10.1785/0120090253.

Zinke, R., J. Hollingsworth, and J. F. Dolan (2014), Surface slip and off-fault deformation patterns in the 2013 M_w 7.7 Balochistan, Pakistan earthquake: Implications for controls on the distribution of near-surface coseismic slip, *Geochem. Geophys. Geosyst.*, *15*, 5034–5050, doi:10.1002/2014GC005538.

Zweck, C., J. T. Freymueller, and S. C. Cohen (2002), Three-dimensional elastic dislocation modeling of the postseismic response to the 1964 Alaska earthquake, *J. Geophys. Res.*, *107*(B4), 2064, doi:10.1029/2001JB000409.